

VELOCITY FIELDS IN LATE-TYPE GALAXIES FROM H α FABRY-PEROT INTERFEROMETRY. II. KINEMATICS AND DYNAMICS OF THE Sd SPIRAL NGC 7793

E. DAVOUST¹ AND G. DE VAUCOULEURS

Department of Astronomy and McDonald Observatory, The University of Texas at Austin

Received 1980 April 2; accepted 1980 May 13

ABSTRACT

The velocity field in the SA(s)d spiral NGC 7793 at a distance $\Delta = 3.1$ Mpc in the Sculptor group is derived from 3822 velocities measured on 21 H α interferograms taken with the Galaxymeter attached to the 92 cm and 205 cm reflectors of McDonald Observatory. A catalog of 132 H II regions is presented. The number density of H II regions decreases roughly exponentially with radial distance in the plane of the galaxy.

Isovelocity maps at 12" and 24" resolution are presented. Analysis of the velocity field gives an inclination $i = 53^\circ$ in good agreement with the photometry, but the position angle of the line of nodes $\theta_0 = 108^\circ$ differs by 11° from the photometric major axis in p.a. 97° . The center of rotation coincides with the optical nucleus and the systemic velocity $V_s = 221 \pm 1$ km s⁻¹ is in excellent agreement with other recent optical and radio determinations. The maximum rotation velocity $V_M = 95$ km s⁻¹ at $R_M = 4.1 = 3.7$ kpc is in good agreement with the value (96) expected from the luminosity index $\Lambda_c = 1.34$ of the galaxy.

The masses estimated by fitting the observed rotation curve to various conventional mass distribution models—neglecting velocity dispersion—are in the range $8 < \mathfrak{M}_T < 16 \times 10^9$ solar units, of which 2–4% is in a small spheroidal component. A more satisfactory fit in better agreement with the photometry was obtained with a two-component generalized Toomre model—including velocity dispersion—following Miyamoto and co-workers. The best fit model has a total mass $\mathfrak{M}_T = 8.9 \times 10^9$ solar masses of which 3.4% is in the spheroid. The velocity dispersion at the center is $\sigma_r = 40$ km s⁻¹, in good agreement with the value (45) expected for the absolute magnitude (-13.24) of the small bulge component of NGC 7793 if it obeys the $\mathfrak{L} \propto \sigma_r^4$ relation valid for ellipticals. The mass-to-blue luminosity ratio is $\mathfrak{M}_T/\mathfrak{L}_T(B) = 2.74$, with 6.59 for the bulge component and 2.68 for the disk component. There is no clear indication of significant noncircular motions except perhaps in the northeast outer regions of the disk.

Subject headings: galaxies: individual — galaxies: internal motions — galaxies: stellar content — interferometry — nebulae: general

I. INTRODUCTION

NGC 7793 is a late-type ordinary spiral (Fig. 1 [Plate 1]), the SA(s)d prototype (Shapley 1943), and the fifth brightest member of the Sculptor group (de Vaucouleurs 1959). Its inclination, large apparent diameter, numerous H II regions, and widespread H α emission in the disk (Monnet 1971) make it an ideal object for a study of the velocity field by Fabry-Perot interferometry. A detailed photometric analysis of this galaxy was previously reported in the series "Southern Galaxies" (de Vaucouleurs and Davoust 1980, hereafter SG VIII) to serve as an introduction to the present study of the velocity field. The luminosity distribution is dominated by the exponential disk contributing 98.6% of the total B luminosity, 65.4% arising from the underlying old disk component and 33.2% from the young arm component. The spheroidal $r^{1/4}$ component contributing 1.4% with an effective radius $r_e^I = 6''.00 = 0.09$ kpc is detectable only near the nucleus.

The distance corresponding to the revised modulus $\mu_0 = 27.48 \pm 0.25$ is $\Delta = 3.13 \pm 0.38$ Mpc, and the scale factor $l' = 0.91$ kpc. The corrected (face-on) absolute magnitude is $M_T^0 = -18.35$ ($\log \mathfrak{L}/\mathfrak{L}_\odot = 9.512$, if $M_G^0 = +5.43$), and the effective radius $r_e = 2.11 = 1.92$ kpc. NGC 7793 is intermediate in luminosity between M33 (-18.51) and the LMC (-18.17), but it is 25% smaller and consequently its average B surface brightness is ~ 0.5 mag greater.

¹On leave from Observatoire de Besançon, France.

A preliminary rotation curve from optical interferometry has been reported by Carranza and Agüero (1977) at Cordoba, and low-resolution radio studies in the 21 cm line by Gouguenheim (1969) and Gouguenheim and Bottinelli (1979) at Nançay and by Whiteoak and Gardner (1977) at Parkes.

II. OBSERVATIONS

The velocity field was derived from 21 H α image tube interferograms taken with the previously described Galaxymeter system (de Vaucouleurs and Pence 1980, hereafter Paper I) attached at the Cassegrain foci of the 91 cm and 205 cm McDonald reflectors. The plate scales are 78" and 34".3 mm⁻¹, and the field of view 7' and 3'.5, respectively. The free spectral range with the No. 2 etalon (FP2) is 6 Å = 282 km s⁻¹. A 10 Å FWHM interference filter placed in the parallel beam in front of the etalon was used to isolate the H α line. Well-exposed fringes were recorded in 30–45 minutes on preflashed 103a-G film with the CO₂ gas-cooled two-stage S20VR 25 mm Varo tube operated at 20–24 kV. The observing log is in Table 1. Examples of interferograms are reproduced in Fig. 2 (Plate 2).

Since the etalon was used $\sim 5^\circ$ off axis to approximate a multislit spectrograph, the fringes run roughly north-south when the *Ox* axis of symmetry of the fringe pattern is in p.a. 270°. To improve the coverage, interferograms were also obtained with the *Ox* axis in p.a. 180° and 225° so as to crisscross the galaxy with fringes. This resulted in a fairly uniform distribution of 3822 velocity points (Fig. 3) within the total field of 5'.25 \times 4'.25 where measurable fringes were recorded. This field roughly corresponds to regions brighter than $\mu_B \approx 23$ mag arcsec⁻².

In order to assist in the rejection of continuum sources and stars and to help prepare a catalog of discrete H II regions (§ III), two photographs (one with each telescope) were taken through the H α filter (centered at 6567 Å) and one through a 10 Å filter (centered at 6552 Å) excluding H α .

III. THE H II REGIONS

Since the positions of H II regions were needed as reference points (§ IV), it was found useful to identify most H II regions of the galaxy, determine their position accurately, and establish a catalog. The H II regions of this galaxy have also been discussed by Monnet (1971), Carranza and Agüero (1977), and Hodge (1969a).

a) Catalog and Map

Two H α films were available for the identification of H II regions, one at low resolution (IFP 30 with 91 cm reflector), one at high resolution (IFP 150 with 205 cm reflector). In addition, one high resolution film in the

TABLE 1
FABRY-PEROT INTERFEROGRAMS OF NGC 7793

Galaxy Film	Calibration Film	Date (UT)	Reduction to Sun	p.a. (OX) (degrees)	Field Center
FP2 108	FP2 123	721013	-15.17	270	Nucleus
FP2 109	"	"	-15.17	270	7".5 E
FP2 110	"	"	-15.17	270	15" E
FP2 111	"	"	-15.17	270	2' E
FP2 112	"	"	-15.17	270	2' W
FP2 127 ^a	b	721102	-21.55	270	Nucleus
FP2 128 ^a	FP2 131	721103	-21.81	270	16".5 E
FP2 129 ^a	"	"	-21.81	270	33" E
FP2 130 ^a	"	"	-21.81	270	50" E
FP2 138 ^a	FP2 141	721104	-22.06	270	4' W
FP2 333	FP2 337	751030	-20.73	180	Nucleus
FP2 334	"	"	-20.73	180	1'.5 N
FP2 335	"	"	-20.73	180	1'.5 S
FP2 345	FP2 344	721031	-21.02	180	1'.5 W
FP2 346	"	721031	-21.02	180	1'.5 E
FP2 347	"	751031	-21.02	180	3'.0 E
FP2 413	FP2 416	771011	-14.42	225	Nucleus
FP2 414	"	"	-14.42	225	1'.5 S, 1'.75 W
FP2 415	"	"	-14.42	225	1'.5 N, 1'.75 W
FP2 418	FP2 420	771012	-14.80	225	1'.5 N, 1'.5 E
FP2 419	FP2 420	771012	-14.80	225	1'.5 S, 1'.5 E

^a91 cm reflector.

^bFor FP2 127 the calibration film for the following night was used (i.e., FP2 131).

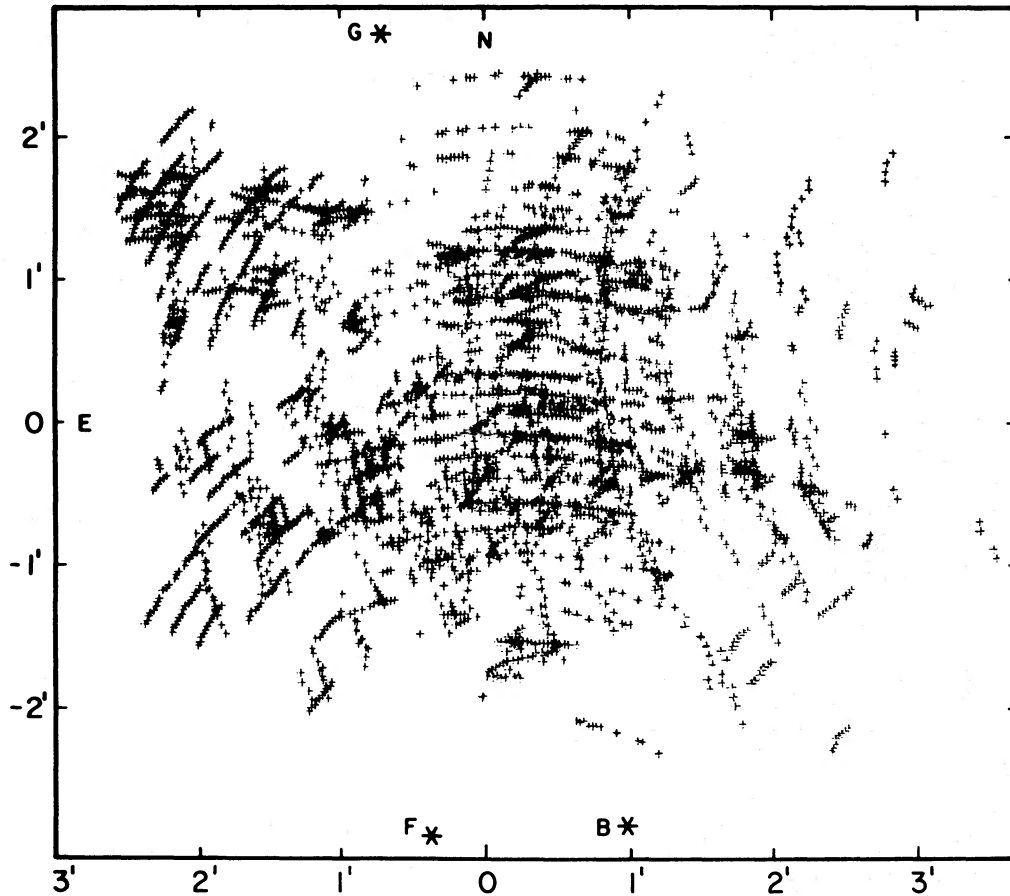


FIG. 3.—Distribution of 3822 velocity points measured on 21 interferograms of NGC 7793. Three field stars are marked.

continuum just outside $H\alpha$ (IFP 151) was used to identify foreground stars (i.e., continuum sources). Foreground stars in the outer regions not covered by IFP were identified on the basis of high surface brightness and small size.

The positions of the $H\ II$ regions centers were measured on a two-coordinate comparator. In some instances of extended or elongated nebulae there may be some uncertainty in the position, as can be seen in the comparison with the catalog of Hodge (§ III b). A qualitative estimate of the size and brightness of the various $H\ II$ regions was also made.

The catalog is given in Table 2. The objects are numbered in order of increasing right ascension (col. [1]). An estimate of the size and brightness is given in column (2); bright extended (BE) or compact (BC), medium intensity and extended (E) or compact (C), faint (F). X and Y are the coordinates with respect to the nucleus in arcsec: X increases to the east, Y to the north. The number and coordinates (reduced to our system, see below) in Hodge's catalog are given next. The quantities r and θ are the polar coordinates in the plane of the galaxy, centered on the nucleus, r in kpc, θ increases counterclockwise from the western side of the major axis. To deproject the galaxy, we adopted the inclination (53°) and position angle of the kinematical line of nodes (108°) determined below (§ V c). The coordinates of eight foreground stars are given at the end of the table.

The map of $H\ II$ regions is in Figure 4. The dashed circle indicates the area $4'.3$ in diameter covered by the high resolution film IFP 150. Outside this circle identifications and brightness estimates are less reliable because of the lower resolution of IFP 30 film.

b) Comparison with Hodge

A catalog of 35 $H\ II$ regions has been published by Hodge (1969a); a comparison is possible for 32 objects in common. We have reduced the coordinate system of Hodge to ours by the following transformation: a rotation of $-1'.18$, a translation of $-0''.85$ in X and $+0''.38$ in Y , and a scaling of 0.9963.

TABLE 2
CATALOG OF H II REGIONS IN NGC 7793

<i>N</i>	Class	<i>X</i>	<i>Y</i>	Hodge <i>N</i>	<i>X</i>	<i>Y</i>	<i>R</i>	θ
1..	F	-230.5	31.9	3.62	343.5
2..	BE	-174.4	108.0	35	-170.0	110.0	3.26	22.2
3..	F	-166.2	42.8	2.61	354.1
4..	C	-161.8	103.9	3.08	23.6
5..	F	-155.8	34.1	2.44	350.7
6..	F	-148.4	43.6	2.35	357.3
7..	BC	-148.4	-39.7	2.87	312.9
8..	BE	-142.6	-51.4	34	-143.0	-48.0	2.96	307.8
9..	F	-137.8	-81.0	3.42	298.1
10..	BC	-133.1	-28.8	32	-132.0	-27.0	2.48	315.9
11..	BC	-123.9	-73.0	31	-121.0	-73.0	3.08	298.0
12..	BE	-114.2	-0.7	30	-115.0	-4.0	1.88	331.1
13..	BE	-109.4	-21.8	29	-110.0	-22.0	2.02	317.0
14..	BE	-108.1	39.0	27	-107.0	40.0	1.74	3.0
15..	C	-107.0	-0.8	28	-106.0	-4.0	1.76	331.1
16..	F	-103.5	9.3	1.64	339.3
17..	E	-99.4	-105.7	3.44	285.8
18..	E	-93.4	-110.8	26	-95.0	-109.0	3.48	283.7
19..	C	-87.5	50.2	1.59	19.2
20..	BE	-83.4	-20.4	25	-83.0	-20.0	1.59	314.2
21..	F	-79.2	88.2	2.16	43.9
22..	F	-74.8	7.6	1.19	340.3
23..	E	-74.0	-64.5	2.26	289.8
24..	E	-73.5	52.6	1.48	27.8
25..	BE	-68.3	-23.3	24	-67.0	-23.0	1.40	308.8
26..	F	-65.8	52.5	1.41	32.0
27..	BC	-63.1	63.8	1.59	40.6
28..	E	-56.7	-33.5	1.41	298.0
29..	F	-52.4	108.9	2.54	60.1
30..	BC	-51.8	54.5	1.35	42.0
31..	F	-49.5	67.8	1.61	50.2
32..	E	-48.1	-31.6	1.26	295.7
33..	BC	-47.7	-22.3	1.08	302.7
34..	BC	-46.0	-4.2	0.79	324.5
35..	E	-43.2	26.8	0.81	22.3
36..	BE	-40.9	-33.6	23	-41.0	-38.0	1.21	291.0
37..	F	-40.0	7.4	0.63	347.7
38..	F	-37.2	85.8	2.00	62.0
39..	F	-34.6	114.4	22	-34.0	115.0	2.68	67.3
40..	E	-33.0	-5.8	0.60	318.5
41..	F	-32.7	3.5	0.52	340.7
42..	E	-29.4	-15.7	0.70	300.0
43..	F	-27.6	-81.2	2.16	270.5
44..	E	-26.6	59.8	1.39	61.6
45..	F	-26.5	41.6	0.98	53.8
46..	E	-25.7	-37.5	1.12	280.1
47..	C	-23.1	143.6	3.42	72.9
48..	F	-22.9	-63.2	1.69	271.2
49..	BC	-21.2	-47.4	21	-20.0	-48.0	1.30	273.7
50..	F	-20.8	103.4	2.45	71.3
51..	F	-20.6	77.2	1.81	68.7
52..	E	-20.4	58.2	1.36	65.4
53..	E	-16.8	-93.2	20	-16.0	-96.0	2.37	265.3
54..	F	-15.9	41.3	0.96	64.0
55..	E	-14.3	53.1	19	-18.0	54.0	1.25	68.6
56..	F	-13.9	70.9	1.68	71.5
57..	F	-13.0	63.5	1.50	71.1
58..	F	-12.9	77.2	1.84	72.6

TABLE 2—Continued
 CATALOG OF H II REGIONS IN NGC 7793

<i>N</i>	Class	<i>X</i>	<i>Y</i>	Hodge <i>N</i>	<i>X</i>	<i>Y</i>	<i>R</i>	θ
59..	F	-12.6	-7.0	0.31	299.2
60..	F	-9.6	25.0	0.58	64.0
61..	E	-6.8	-102.1	2.53	261.3
62..	F	-2.7	-55.3	1.37	260.7
63..	F	0.1	-48.1	1.17	258.8
64..	BC	0.5	-20.2	0.49	258.1
65..	F	1.0	73.9	1.81	79.4
66..	E	4.3	49.3	1.23	82.1
67..	F	4.3	23.9	0.61	85.3
68..	C	8.3	-36.4	0.86	250.2
69..	F	8.7	42.0	1.08	86.2
70..	F	10.0	-3.0	0.16	177.7
71..	C	11.0	-63.9	1.52	252.4
72..	F	11.8	-25.2	0.59	240.7
73..	BC	13.5	69.9	15	16.0	72.0	1.79	85.7
74..	BC	14.1	-80.9	17	15.0	-82.0	1.92	252.3
75..	E	18.5	22.9	0.71	102.9
76..	F	19.2	-0.7	0.31	154.8
77..	E	20.3	-12.1	0.37	200.9
78..	C	21.9	-44.2	1.03	239.5
79..	E	26.1	-60.5	1.41	242.1
80..	E	27.6	15.9	14	29.0	15.0	0.68	118.4
81..	E	27.9	-66.8	1.56	242.6
82..	E	28.7	5.3	0.52	137.9
83..	F	35.9	-57.4	1.35	234.4
84..	F	38.5	5.3	0.68	141.1
85..	C	39.0	12.4	0.78	130.0
86..	C	41.7	-12.7	0.66	178.3
87..	F	42.3	-64.6	1.52	233.2
88..	C	46.1	-76.4	13	44.0	-77.0	1.79	235.2
89..	F	46.9	-35.6	0.97	210.0
90..	F	48.0	48.0	1.59	107.1
91..	C	49.9	-25.1	0.86	194.3
92..	BE	53.0	39.2	11	52.0	38.0	1.47	113.3
93..	BC	54.3	-38.3	12	53.0	-40.0	1.08	207.2
94..	F	58.3	47.0	1.70	111.5
95..	BC	58.5	86.2	9	58.0	87.0	2.56	99.9
96..	F	61.1	-15.8	0.96	174.2
97..	BE	63.3	-3.7	10	60.0	-4.0	1.02	156.5
98..	BC	64.5	-90.0	8	65.0	-92.0	2.14	230.8
99..	C	67.7	-50.0	1.38	208.9
100..	C	69.4	51.9	1.94	113.0
101..	E	70.5	86.9	2.70	103.0
102..	F	72.0	-16.0	1.13	170.9
103..	F	74.6	11.6	1.33	139.9
104..	BC	76.8	-112.2	2.65	232.0
105..	C	77.2	12.7	1.39	139.4
106..	E	77.3	44.2	1.89	118.7
107..	BC	79.8	-14.8	1.25	167.7
108..	E	82.4	9.1	1.43	143.1
109..	E	84.9	-43.3	1.48	194.8
110..	BC	90.7	-43.3	7	88.0	-44.0	1.55	192.4
111..	E	91.8	97.7	6	92.0	98.0	3.18	105.8
112..	BC	94.3	50.0	2.24	120.2
113..	BC	96.1	56.5	2.38	118.1
114..	F	100.7	87.2	3.06	110.0
115..	C	105.4	49.2	2.38	122.8

TABLE 2—Continued
CATALOG OF H II REGIONS IN NGC 7793

<i>N</i>	Class	<i>X</i>	<i>Y</i>	Hodge <i>N</i>	<i>X</i>	<i>Y</i>	<i>R</i>	θ
116..	F	106.9	-19.4	1.67	167.3
117..	BC	114.4	-79.1	2.26	206.4
118..	BC	116.7	-83.7	2.35	207.8
119..	E	123.0	-7.9	1.97	157.0
120..	F	126.0	-54.2	2.10	188.7
121..	C	129.5	-7.9	2.07	156.7
122..	E	131.1	100.6	5	130.0	102.0	3.72	112.5
123..	E	133.1	121.6	4	132.0	121.0	4.18	108.9
124..	E	134.2	75.3	3.26	119.0
125..	E	136.9	73.4	3.26	120.0
126..	F	136.9	32.7	2.60	134.5
127..	E	138.0	39.4	2.71	131.8
128..	E	139.2	50.7	2.90	127.6
129..	E	142.6	88.1	3.62	117.0
130..	E	145.9	106.5	3	144.0	109.0	4.02	113.5
131..	E	148.3	93.4	3.80	116.6
132..	BE	213.6	29.7	3.78	141.1
Stars								
A	-174.5	-9.5
B....	...	-58.5	-168.5
C....	...	-11.9	34.3
D	-10.6	174.3	18	-8.0	177.0
E....	...	10.1	180.0
F....	...	20.4	-173.3	16	20.0	-177.0
G	43.1	163.9
H	210.0	-233.1

The mean distance between Hodge's positions (after transformation) and our positions is $\langle \delta \rangle = 2''.29$ with a standard deviation $\sigma(\delta - \langle \delta \rangle) = 1''.24$.

Two of Hodge's objects (Nos. 16 and 18) were identified as stars by us. His objects 1 and 2 were outside the field of our H α films.

c) Density Distribution

Previous studies of the radial distribution of H II regions in spiral galaxies have shown that there is a peak in the number of nebulae at about one-fourth the distance from the center to the farthest H II regions (Hodge 1969*b*) and that the number density tends to fall off either exponentially (Kennicutt and Hodge 1976) or as $1/r$ (Boeshaar and Hodge 1977). The latter is the falloff produced by a logarithmic spiral with uniform distribution of H II regions along the arms.

The radial distribution $\nu(r)$ of the number density of H II regions is given in Table 3 and shown in Figure 5*a*. The peak in the number distribution occurs farther out than predicted by the $1/r$ law (*dotted line*), and the falloff in $\nu(r)$ is better fitted by an exponential except near the center (*dashed line*).

The distribution of H II regions was compared to the luminosity distribution of the various components. The surface brightness of the old disk (α) (eq. [4] of SG VIII) was converted to specific intensities I_α ; the intensity of the arm component (I_β) was obtained by dividing the total intensity of the arms in concentric rings by the area of the rings. The ratio of the number density $\nu(r)$ of H II regions to specific intensities exhibits a broad maximum around $r=1$ kpc and decreases slowly outward (Fig. 5*b*). This confirms that the number density of H II regions decreases exponentially together with the disk intensity.

These conclusions are only tentative because the sample of H II regions is small and complete only out to $r=2.3$ (in projection), or about 2.5 kpc in the plane of the galaxy (the last four bins contain the 30 objects that were detected outside the high resolution film).

IV. REDUCTION OF INTERFEROGRAMS

The reduction of the interferograms followed the procedures described in Paper I. The normal procedure to reduce the films to a common reference system is to use foreground stars of known positions. In the case of NGC 7793 there

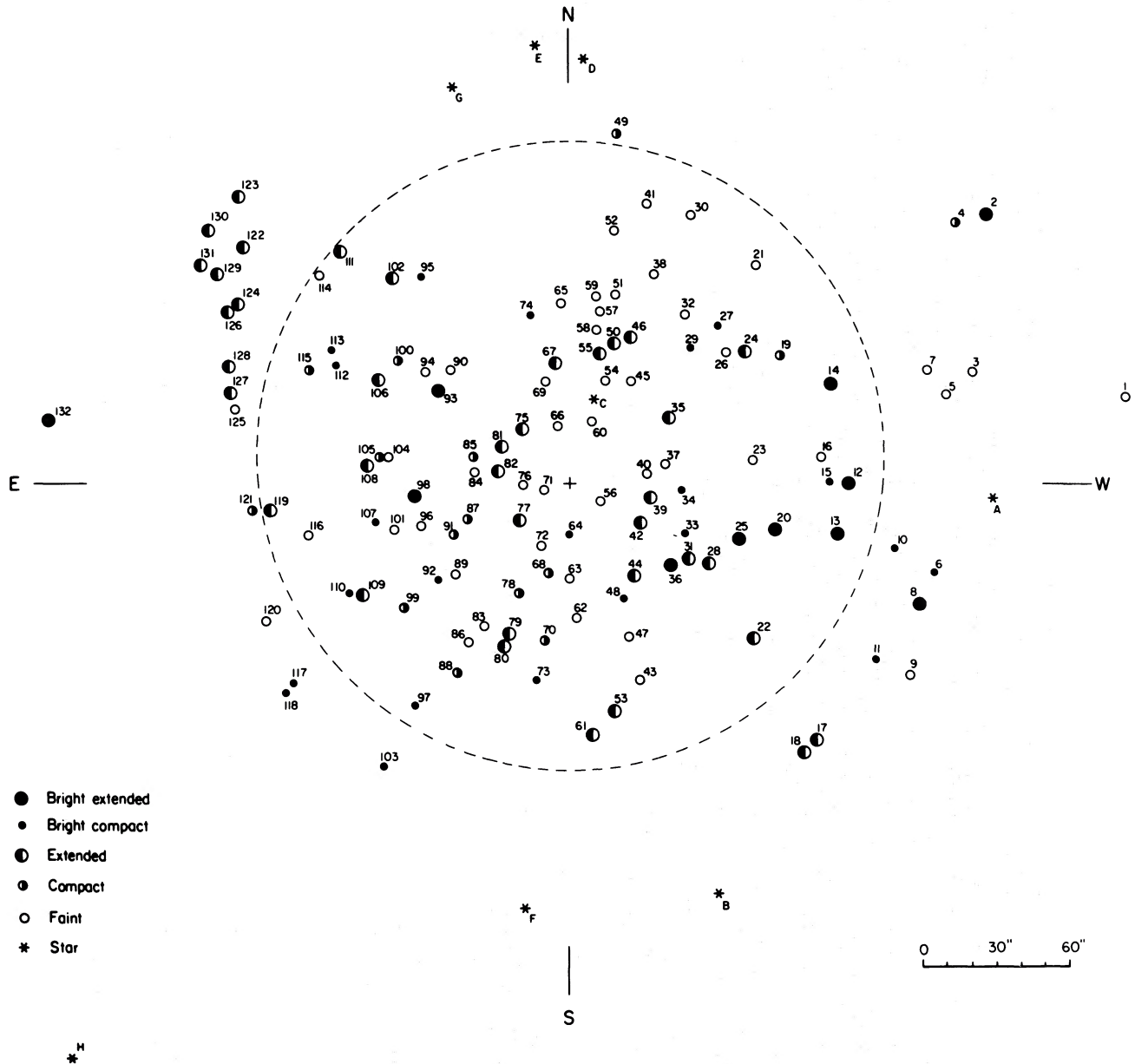


FIG. 4.—Distribution of 132 H II regions in NGC 7793. Dashed circle $4\frac{1}{3}$ in diameter shows area covered by high-resolution film where identifications and brightness estimates are reliable.

are only two foreground stars, one of which was seen on a few films only. In the absence of reference stars we tried to identify as many H II regions as possible on the films and used them to combine the films. H II regions are not point sources or continuum sources: great care had to be exercised to identify a bright knot on a fringe with an H II region and determine the position of its center. We were able to use up to 10 H II regions per film, and the mean error in the reduction of each film to the common system was not larger than $3''$ with a mean around $2''$. As an independent check we used the positions and orientations of the films recorded in the logbook as well as the expected velocity gradient.

Once all velocity points were brought to the same system of coordinates, the galaxy was divided into $12''$ square resolution elements. A mean velocity was attributed to each pixel and the mean residual velocity (MRV) of each film with respect to the mean velocity field was computed. Two films, 414 and 418, stood out with rather large MRVs of 13.07 and 13.22 km s^{-1} , respectively, or 20.4 and 28.7 km s^{-1} , respectively, if the mean velocity field did not include

TABLE 3
DISTRIBUTION OF H II REGIONS COMPARED TO LUMINOSITY DISTRIBUTION IN GALAXY

$R(\text{kpc})$	N	ν	$I_{\text{H}}^{(\alpha)}$	$I_{\text{H}}^{(\beta)}$	$\nu/I_{\text{H}}^{(\alpha)}$	$\nu/I_{\text{H}}^{(\beta)}$	ν/I_{H}
0.0–0.5 ...	5	6.37	212.03	39.25	3.00	16.23	2.54
0.5–1.0 ...	21	8.91	140.35	20.29	6.35	43.92	5.55
1.0–1.5 ...	31	7.89	92.90	25.94	8.49	30.41	6.64
1.5–2.0 ...	27	4.91	61.49	26.55	7.99	18.49	5.58
2.0–2.5 ...	18	2.55	40.70	21.31	6.27	11.97	4.11
2.5–3.0 ...	12	1.39	26.94	17.41	5.16	7.985	3.13
3.0–3.5 ...	11	1.08	17.83	9.338	6.06	11.57	3.98
3.5–4.0 ...	5	0.42	11.80	6.385	3.56	6.578	2.31
4.0–4.5 ...	2	0.15	7.81	5.044	1.92	2.974	1.17

EXPLANATION.— N , number of H II regions; ν ; number density of H II regions (per kpc²); $I_{\text{H}}^{(\alpha)}$ and $I_{\text{H}}^{(\beta)}$ are specific intensities of old Population I disk and arm components (from de Vaucouleurs and Davoust 1980) in $\mathcal{L} \text{ pc}^{-2}$; $\nu/I_{\text{H}}^{(\alpha)}$, $\nu/I_{\text{H}}^{(\beta)}$, and ν/I_{H} are in 10^{-8} H II regions/ \mathcal{L}_{\odot} .

these two films. Furthermore, the fringes produced by the OH $\lambda 6577.1$ night-sky line on the two films displayed Doppler shifts of 28 and 35 km s⁻¹, respectively. No such zero-point shift was detected on other films. After checking for possible sources of error, it was decided to apply a systematic correction of -25 km s⁻¹ to all velocities from both films.

One may question the validity of this correction for film 418 in view of the residual velocities (of up to -15 km s⁻¹) on the eastern edge of the velocity field (see § VII c). However, while these residual velocities would vanish if one did not apply the correction, the positive residuals in the northeast would be greatly enhanced.

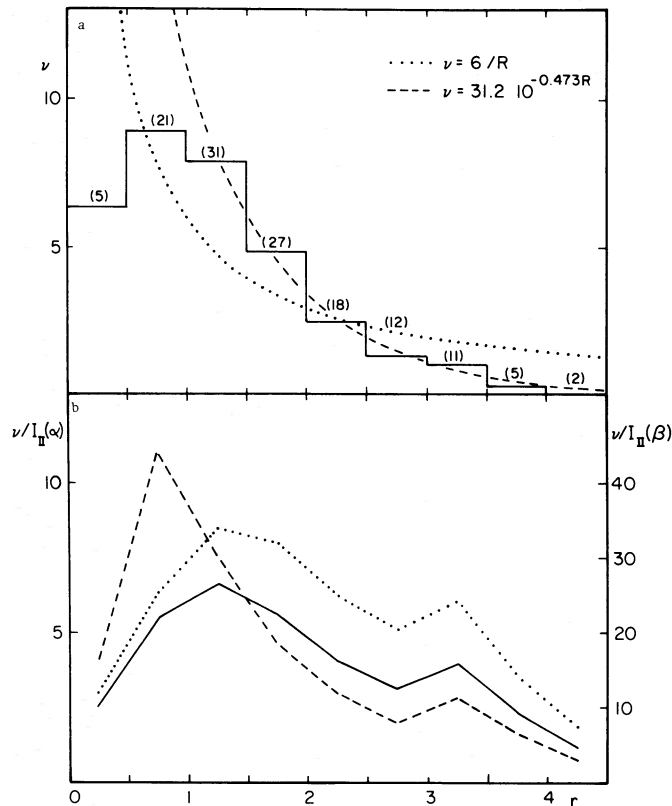


FIG. 5.—Distribution of H II regions in plane of NGC 7793. (a) Number density $\nu(r)$ versus radius r in kpc. Exponential (dashed line) gives better fit at $r > 1$ kpc. Number N of H II regions in each bin is given in parentheses. (b) Ratio of surface density ν to specific intensity I of disk (solid line, left scale); dotted and dashed lines (right scale) give ratios to old disk $I(\alpha)$ and young (arm) component $I(\beta)$.

TABLE 4
ADJUSTMENT OF FILMS

Film (1)	N (2)	$\langle V \rangle$ (3)	$\langle \Delta V \rangle$ (4)	$\sigma(\Delta V)$ (5)	n (6)
FP2 108	95	216.5	7.58	12.79	10
109	85	202.8	0.42	13.28	5
110	109	212.4	0.56	10.67	5
111	34	163.0	-6.61	15.25	6
112	82	274.5	1.15	11.28	6
127	157	222.8	4.82	12.88	5
128	200	214.6	2.01	12.21	6
129	153	215.2	-1.48	12.13	5
130	202	220.3	2.94	11.57	8
138	88	261.7	-4.87	13.26	5
333	440	239.5	-0.90	15.58	6
334	247	244.9	2.39	12.94	6
335	502	215.3	-5.60	15.10	7
345	195	256.5	-0.51	11.56	6
346	154	204.8	-1.71	12.93	10
347	132	184.4	-3.42	14.63	7
413	197	218.7	1.41	15.28	7
414 ^a	129	251.1	-1.10	12.36	8
415	82	269.3	4.74	12.06	4
418 ^a	274	199.1	0.44	12.45	5
419	264	178.8	3.87	11.73	7
Total ...	3822				

^aAfter zero point correction of -25 km s^{-1} (see text).

EXPLANATION OF COLUMNS.—(1) film number; (2) N , number of velocity points; (3) $\langle V \rangle$, mean velocity of film (km s^{-1}); (4) $\langle \Delta V \rangle$, mean residual velocity of film; (5) $\sigma(\Delta V)$, rms residual velocity of film; (6) n , number of H II regions used as coordinate reference points.

Table 4 gives the parameters obtained in the final adjustment. The unsmoothed velocity field is shown in Figure 6. The velocity gradient is positive from east to west. The near side of the galaxy is south (from the photometry, SG VIII); hence the rotation is counterclockwise and the spiral arms (or arcs) are trailing.

V. THE VELOCITY FIELD

a) The Velocity Map

The velocity field at $12''$ resolution (without interpolation or smoothing) is shown in Figure 6 superposed on a B photograph of the galaxy. It indicates which parts of the galaxy gave measurable H α emission. Much of the detail is probably due to noise rather than velocity anomalies.

An interpolated velocity was then computed for empty pixels which has at least four nonempty neighbors, and a Gaussian-weighted 3×3 smoothing was performed. Figure 7 (Plate 3) shows the resulting velocity field, which was used in the subsequent analysis.

The isovelocity contours have the typical pattern arising in a disk galaxy in differential rotation. From the general symmetry of the pattern it can be seen that the position angle of the line of nodes is slightly larger than 90° . There is some indication in the shape of the outer contours that the maximum rotation velocity is reached near the limits of the measured H α emission. There is evidence for noncircular motions in the northeastern part of the galaxy: the isovelocity contours clearly bend over too much in that region. Finally, the gradient close to the nucleus on the eastern side of the galaxy is steeper, as the contours are closer there.

b) Method of Analysis

The basic assumption in our analysis of the velocity field is that the only mean motion in the galaxy is coplanar circular rotation: the observed radial velocities are mean rotation velocities projected on the line of sight. Noncircular motions and departures from coplanarity will be considered as negligible in a first approximation. The good fit of a model based on this assumption will justify it *a posteriori*.

The method outlined by Warner, Wright, and Baldwin (1973) and Bosma (1978) for the analysis of 21 cm line observations has been adapted to the present case: trial values are assumed for the inclination i , position angle of the

major axis θ_0 , systemic velocity V_s , and position of the rotation center (x_0, y_0) . The galaxy is then deprojected, divided into circular annuli of equal width, and the mean circular velocity $V_{c,k}$ in annulus k is computed from the velocity points falling in this annulus. Each radial velocity V_j in the annulus is weighted by $|\cos \theta'_j|$, where $\theta'_j = \theta_j - \theta_0$ is the angle between the velocity point and the major axis, i.e.,

$$V_{c,k} = \frac{1}{\sin i} \frac{\sum_j [(V_j - V_s) |\cos \theta'_j| / \cos \theta'_j]}{\sum_j |\cos \theta'_j|} = \sum_j \alpha_j (V_j - V_s). \quad (1)$$

Less weight is given to velocity points near the minor axis because there the observational errors are greatly enhanced by the $\sec \theta'_j$ deprojection factor.

The adopted values of the parameters i , θ_0 , V_s , (x_0, y_0) are those which minimize the dispersion around the mean *projected* rotation curve. The dispersion around the mean deprojected rotation curve cannot be used since it depends on inclination; also, the $V_{c,k}$ do not have a Gaussian distribution of errors. In the absence of noncircular motions each observed radial velocity V_j is related to the mean rotation velocity V_c in bin k through

$$V_j - V_s = V_c \sin i \cos \theta'_j, \quad (2)$$

with an error which is due to the observational uncertainties, and to the finite width of the annular zone k . The latter causes a smoothing which may be included in the observational errors. Fitting a continuous curve to the discrete $V_{c,k}$ would not eliminate this error, which is inherent in the way the rotation curve was obtained in the first place. This smoothing can be reduced by taking narrower annuli, but a compromise must be made between the width of each annulus and the number of velocity points per annulus.

The variance to be minimized is

$$\sigma^2 = \frac{1}{N-L} \sum_k \sum_j (V_j - V_s - V_{c,k} \sin i \cos \theta'_j)^2, \quad (3)$$

where L is the number of free parameters. In principle we should compute a dispersion for each annulus since each $V_{c,k}$ has its own error, but this error is an order of magnitude smaller than that on V_j since $V_{c,k}$ is already an average. A rejection cycle can be introduced if the data have too large a dispersion or aberrant points. The effects of the four parameters i , θ_0 , V_s , and (x_0, y_0) on the velocity field cannot be uncoupled, and the search for the loci of minimum dispersion must be made in an iterative way.

It may be useful to compute the dispersion in each annulus given by

$$\sigma_k^2 = \frac{1}{N_k - 1} \sum_j (V_j - V_s - V_{c,k} \sin i \cos \theta'_j)^2 \quad (4)$$

in order to examine whether the loci of minimum dispersion are affected by a large scatter or by systematic trends (e.g., inclination varying with radial distance). However, as the assumed orientation of the galaxy changes, the dispersion in each annulus will vary not only because of the different projection factors but also because the annulus will not include the same velocity points. This fact weakens the validity of this particular analysis unless the annuli are wide enough.

Finally, the standard deviation of each velocity point from the mean velocity curve in the plane of the galaxy is given by

$$s_k^2 = \sum_j \alpha_j^2 \sigma^2 = \frac{\sigma^2 N_k}{\sin^2 i \left(\sum_j |\cos \theta'_j| \right)^2}, \quad (5)$$

where N_k is the number of points in annulus k .

One particular parameter, the position angle θ_0 of the major axis, can also be determined by the method of steepest velocity gradient. This is done by considering a narrow rectangular strip in the observed velocity field and computing the slope dV_r/dr for each position of the strip as it is rotated around the center of symmetry. For solid body rotation (which is mostly the case in the central parts of spiral galaxies) the gradient will be maximum along the line of nodes of the galactic plane with the tangent plane where the projection factor $\cos \theta$ is largest. The position angle θ_0 is found by fitting a sine curve to the data as a function of position angle.

The disadvantage of this method over the preceding one is that it assumes solid body rotation, which in the case of NGC 7793 is true only out to $\sim 50''$ from the center. In the presence of differential rotation the gradient will still be maximum along the line of nodes but shallower, hence more difficult to determine accurately.

It is also possible by this method to check whether the lines of maximum and zero gradients are perpendicular. This is useful to distinguish between oval distortions (axes not perpendicular) and kinematical warps (axes perpendicular), in the case of large scale asymmetries in the velocity field (Bosma 1978).

c) Orientation Parameters

i) Ring Method

An iterative search for the best value of the orientation parameters was made, starting from the values given by the photometry (SG VIII): $i = 53^\circ$, $\theta_0 = 97^\circ$, and a center of rotation at the nucleus, that is, $(x_0, y_0) = (0'', 0'')$. The range of the search was $41^\circ < i < 66^\circ$, $91^\circ < \theta_0 < 126^\circ$, and $\pm 20''$ from the nucleus. The 3822 velocity points were binned in 30 annuli, each $10''$ wide with up to 290 velocity points per annulus, and the minimum of the dispersion computed by equation (3) was searched for, after a two-sigma rejection cycle.

The systemic velocity and the position of the center of rotation must be searched for simultaneously. The position of the center of rotation is located more precisely along the line of nodes where the velocity gradient is largest. The hump near $60''$ on both sides of the rotation curve (Fig. 9) is very useful in determining x_0 . The minimum in the dispersion for displacements perpendicular to the line of nodes is more shallow, and the uncertainty in y_0 is consequently large. However, this has no incidence on the accuracy of V_s which depends only on x_0 . The systemic velocity V_s is the radial velocity at the position of the center of rotation and can be estimated to $\pm 1 \text{ km s}^{-1}$ for each location of the center of rotation. If the center of rotation coincides with the optical center, $V_s = 221 \text{ km s}^{-1}$, in good agreement with other recent optical and 21 cm determinations (see § Ve and Table 10).

The inclination is not well determined by the ring method. The elimination of velocity points within 30° of the minor axis (and hence of the larger residuals in the northeast) yields a shallow minimum in the dispersion of the residuals near $i = 53^\circ$ which we trust to be the correct value for the inclination, since it agrees with the photometric determination (SG VIII). The position angle of the line of nodes is fairly well determined by this method: there is a clear minimum near $\theta = 108^\circ$, whether one uses all data or data near the major axis only. However, this value does not coincide with the position angle of the photometric major axis. The above results may be due to variations of these parameters with radius. This possibility was investigated as follows: the data were binned into $10''$ wide annuli as before to determine the rotation curve, but the galaxy was divided into six $40''$ wide annular zones and the dispersions of residual velocities computed for all data in each zone separately. An estimate of the internal errors can also be obtained in this way. Table 5 gives the results: no trend with radius is evident. The values $i = 53^\circ$ and $\theta_0 = 108^\circ$ are adopted.

ii) Method of Steepest Gradient

The velocity gradient was computed in 18 rectangular strips ($10'' \times 80''$) centered on the nucleus and spaced at 10° in position angle. There were 72 to 110 velocity points in each strip, from three to seven less after a 2 sigma rejection cycle.

The velocity gradients (in $\text{km s}^{-1} \text{ kpc}^{-1}$) are plotted versus position angle θ in Figure 8. The maximum gradient corresponds to the angle $\theta_0 = 100^\circ$ which agrees well with the orientation of the photometric isophotes (SG VIII). A sine curve of equation

$$dV/dr = -76 \cos(\theta - 110^\circ)$$

TABLE 5
INCLINATION AND LINE OF NODES FROM KINEMATICS

Ring	N	θ_0	i	$\theta_0 = 108^\circ$		
				A^a		B^b
				N	i	N
0''-40''	353	109°	51°	369	54°	236
40''-80''	792	107	54	774	55	490
80''-120''	992	109	51	1008	50	580
120''-160''	642	107	58	648	59	348
160''-200''	475	107	58	485	55	203
200''-240''	267	109	47	194	52	45
Total	3521	3478	...	1902
Weighted mean . . .		$107^\circ 9 \pm 1.4$	$53^\circ 7 \pm 3.8$		$54^\circ 0 \pm 3.7$	

^aAll data.

^bData within 60° of line of nodes.

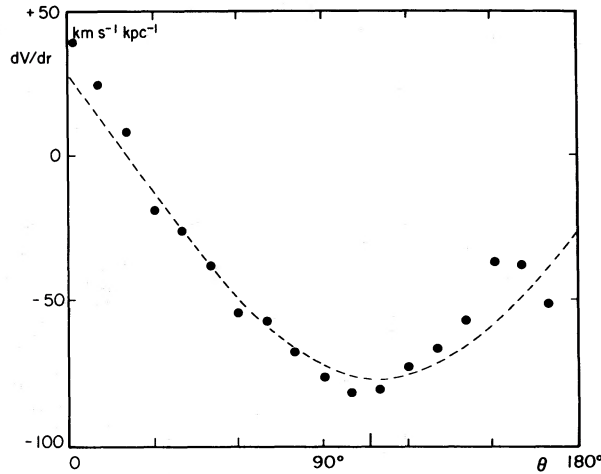


FIG. 8.—Velocity gradient in $10'' \times 80''$ strips versus position angle. The sine curve best fitted by least squares yields a position angle $\theta_0 = 110^\circ$ for the line of nodes.

fitted by least squares to the unweighted data in Figure 8 yields a position angle $\theta_0 = 110^\circ$ for the line of nodes. This value is more reliable since it results from a fit to all data (after a two sigma rejection) and agrees with the value derived above by the ring method.

The orientation parameters and their estimated errors are given in Table 6.

d) The Rotation Curve

The galaxy was deprojected with the set of orientation parameters adopted in § Vc, and the rotation curve derived with the ring method, at different resolutions: rings $20''$, $10''$, and $5''$ wide for all data or for the east or west side of the galaxy only (Tables 7, 8, 9).

TABLE 6
ORIENTATION PARAMETERS FOR N7793

$(x_0, y_0) = (1'' \pm 2'', 0'' \pm 15'')$
$V_s = 221 \pm 1 \text{ km s}^{-1}$
$i = 53^\circ \pm 3^\circ.8$
$\theta_0 = 108^\circ \pm 1^\circ.4$

TABLE 7
EAST AND WEST HALVES OF ROTATION CURVE AT $20''$ RESOLUTION

\bar{r} (arcsec)	West			East			All Points			Points $\theta - \theta_0 < 60^\circ$		
	N	V_c	s_k	N	V_c	s_k	N	V_c	s_k	N	V_c	s_k
12.8.....	48	28.9	1.9	18	19.2	4.5	64	27.9	1.8	47	28.7	1.7
30.4.....	122	45.9	1.2	74	54.3	2.1	196	49.1	1.1	143	45.9	1.0
50.....	133	53.8	1.3	132	52.4	1.4	267	53.4	0.9	172	51.0	0.9
69.....	160	55.5	1.4	151	56.3	1.3	312	56.0	0.9	205	55.9	0.8
89.....	236	62.7	1.2	151	67.1	1.5	384	64.0	1.0	204	64.4	0.9
109.....	240	77.5	1.2	138	70.5	1.2	372	75.4	0.8	232	75.1	0.8
130.....	162	82.0	1.3	107	78.8	1.5	269	81.1	1.1	170	79.7	0.9
150.....	91	86.5	1.9	113	89.0	1.7	198	87.2	1.3	113	85.1	1.3
169.....	78	90.1	2.3	125	81.4	2.4	204	85.5	1.6	100	92.3	1.4
188.....	55	94.9	2.6	58	89.5	4.3	113	93.6	2.3	38	100.9	2.4
209.....	24	89.1	4.3	68	109.0	3.2	84	103.2	2.8	21	93.7	3.7
229.....	30	103.8	6.2	65	126.8	3.0	92	122.5	2.7	14	90.3	5.1
249.....	3	80.6	20.7	47	92.4	3.7	50	92.0	3.5	3	40.7	8.6
268.....	3	70.2	10.3	10	13.6	10.0	9	25.0	10.0	2	74.4	9.9
297.....	5	25.3	13.3	5	25.3	13.8
303.....	3	41.9	18.5	3	41.9	19.1
σ	7.9	8.6	8.2	7.8

TABLE 8
EAST AND WEST HALVES OF ROTATION CURVE AT 10" RESOLUTION

\bar{r} (arcsec)	West			East			All Points			Points at $\theta - \theta_0 < 60^\circ$		
	N	V_c	s_k	N	V_c	s_k	N	V_c	s_k	N	V_c	s_k
5.3...	6	34.2	4.9	8	9.4	5.1	13	25.3	3.6	12	25.6	3.4
15.2...	40	27.5	2.0	10	31.4	7.2	51	28.6	2.1	35	29.6	1.9
25.....	71	45.5	1.6	21	49.1	3.0	94	47.0	1.5	71	43.9	1.4
35.....	49	47.6	1.8	51	57.4	2.9	102	51.2	1.6	70	49.3	1.4
45.....	59	49.6	2.0	64	51.9	2.0	123	50.9	1.4	78	45.0	1.3
55.....	75	55.8	1.7	68	52.1	1.7	143	54.3	1.3	102	54.7	1.1
65.....	76	52.5	1.8	105	56.0	1.6	181	54.6	1.2	125	54.7	1.0
75.....	80	61.4	2.1	47	56.2	2.1	129	59.1	1.5	77	58.4	1.4
85.....	133	55.7	1.6	61	62.7	2.3	196	58.4	1.3	110	60.2	1.2
95.....	101	70.4	1.8	81	67.4	2.1	188	70.2	1.3	96	69.8	1.2
105.....	125	74.5	1.5	83	69.1	1.6	206	72.5	1.0	139	72.5	1.0
115.....	110	82.1	1.9	52	73.2	1.9	167	79.5	1.4	94	78.6	1.2
125.....	92	88.0	1.8	53	75.9	2.0	145	83.5	1.4	86	83.2	1.2
135.....	69	75.8	2.0	57	82.1	2.2	128	78.7	1.5	86	75.5	1.4
145.....	44	80.4	2.8	59	83.7	2.1	106	83.3	1.7	63	82.2	1.6
155.....	44	92.8	2.6	60	97.9	2.8	99	95.2	1.9	50	90.7	1.8
165.....	46	87.8	3.1	84	72.5	3.1	125	79.2	2.3	52	87.4	1.9
174.....	32	90.5	3.1	46	97.7	3.4	80	94.3	2.3	43	98.2	2.2
184.....	38	93.8	3.0	31	94.9	5.8	69	94.2	2.8	27	95.6	2.7
195.....	16	103.4	4.9	27	79.0	6.1	44	92.5	3.9	10	118.4	4.9
205.....	17	85.1	4.7	35	91.8	4.8	51	89.9	3.5	13	84.5	4.1
215.....	8	94.6	8.0	31	122.3	4.2	38	118.6	3.7	10	109.0	5.5
225.....	22	126.9	7.7	25	123.3	4.5	47	124.6	4.0	11	88.8	5.6
234.....	9	56.6	12.1	39	128.2	3.8	44	121.8	3.8	3	96.1	11.0
243.....	1	110.0	...	28	86.5	4.7	28	89.4	4.7	1	51.5	...
254.....	1	56.3	...	19	101.2	5.7	20	99.7	5.5	2	37.0	9.2
266.....	2	67.9	14.0	6	27.2	11.8	8	39.8	9.1	1	75.5	...
272.....	1	73.4	...	4	-30.6	17.2	5	-16.3	14.7	1	73.4	...
...	0	0	0	0
297.....	5	25.3	12.9	0	5	25.3	13.7	0
303.....	3	41.9	17.9	0	3	41.9	18.9
σ	7.7	8.4	8.1	7.7

The rotation curve rises fast to a first plateau near $r = 50''$, then more slowly to a maximum velocity $V_M = 95 \text{ km s}^{-1}$ at $r_M = 4':1$ where our data begin to scatter because the velocity points are fewer and further away from the line of nodes. Figure 9a shows the rotation curve at $5''$ resolution out to $3'$ and at $20''$ resolution beyond. The maximum velocity agrees very well with the value of 96 km s^{-1} expected for a galaxy of luminosity index $\Lambda_c = 1.34$ (SG VIII) which is

$$\log V_M = 2.15 - 0.5(\Lambda_c - 1)$$

(de Vaucouleurs 1977).² However, the radius r_M at V_M found here ($r_M \sim 4'$) does not agree with the value of $7:16$ expected from the empirical relation

$$\log V_M + \log(2r_M/D_0) = 2.18 \pm 0.03$$

(de Vaucouleurs 1977). This relationship may not be valid for late type galaxies where r_M is not well determined.

There are no significant differences between the E and W parts of the rotation curve, shown in Figure 9b for rings $20''$ wide. In particular the plateau near $r = 50''$ is evident on both sides. The larger scatter in the east between $2:5$ and $5'$ is due to the residual velocities in the NE, and is significantly reduced by using only velocity points within 60° of the line of nodes to determine the rotation curve. The initially steeper gradient in the East is not readily seen at this resolution.

²There is an unfortunate misprint in the equation quoted in the original paper, where the coefficient 0.5 is missing.

TABLE 9
MEAN ROTATION CURVE AT 5" RESOLUTION^a

\bar{r}	N	V_c	s_k	\bar{r}	N	V_c	s_k
3.7	6	30.7	5.4	157.6	49	93.7	3.0
6.9	7	20.9	4.8	162.8	61	83.6	2.8
12.6	25	25.1	3.0	167.3	65	74.5	3.7
17.7	27	35.1	2.8	172.2	48	93.5	3.1
22.5	50	46.8	2.0	177.2	32	95.6	3.4
27.5	45	46.5	2.2	182.5	45	98.1	3.8
32.6	50	51.8	2.4	187.3	26	83.5	3.6
37.3	51	51.2	2.1	192.5	15	86.8	6.3
42.3	62	49.2	2.0	198.0	25	95.7	5.5
47.5	62	53.1	2.0	202.7	26	105.3	6.2
52.4	66	54.3	1.8	207.2	29	82.8	4.3
57.2	77	54.3	1.6	212.3	20	114.6	5.2
62.6	93	56.2	1.6	217.2	17	120.5	5.3
67.3	90	53.7	1.6	223.4	24	106.2	5.2
72.8	57	53.7	2.3	227.9	23	126.6	5.7
77.8	68	62.8	2.1	232.6	30	125.2	5.8
82.3	100	54.5	1.9	237.4	16	109.4	5.9
87.6	91	62.5	1.9	243.3	12	92.3	7.1
92.5	91	68.3	2.0	247.6	17	85.1	6.0
97.5	97	71.8	1.8	252.5	10	89.4	7.8
102.4	103	69.0	1.5	257.8	9	107.6	8.1
107.6	107	75.3	1.5	261.7	2	94.6	16.2
112.5	87	75.8	1.8	267.6	6	21.5	12.5
117.7	77	83.8	2.1	273.2	4	-12.9	16.2
122.3	81	85.2	1.8	275.6	2	-85.8	24.6
127.3	62	81.3	2.2	...	0
132.8	63	80.7	1.9	...	0
137.6	66	77.0	2.1	...	0
142.4	56	79.9	2.1	296.8	5	25.3	13.7
147.3	52	85.0	2.6	302.6	3	41.9	18.9
152.7	49	95.9	2.7				

^aAll points.

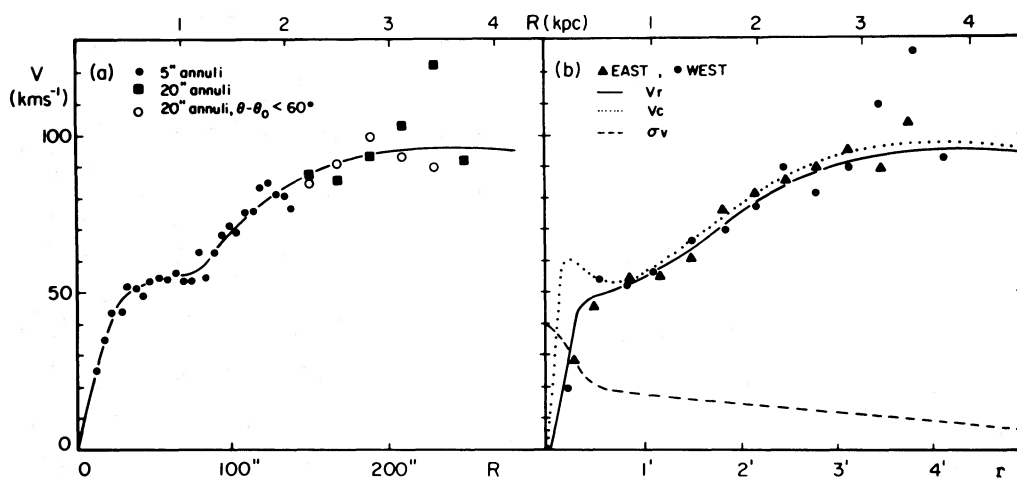


FIG. 9.—Rotation curve of NGC 7793. (a) Mean points at 5" and 20" resolution. (b) Mean points at 20" resolution separately for east and west halves of galaxy. Velocity dispersion σ_v (dashed), circular velocity V_c (dotted) of best fit two-component model, and calculated rotation curve V_r (solid line) are shown.

TABLE 10
COMPARISON WITH OTHER STUDIES

Sources	V_s	θ_0	r_M (arcmin)	V_M (km s ⁻¹)	i	\mathfrak{M}_T
WG (1977)	227	130	3.75	103	45 ^{ob}	27.6
GB (1979)	228		4.8	62	44 ^{ob}	13.0
CA (1977)	215	95	1.1	60	50 ^{ob}	28.0
This study	221	108	4.1	76	53 ^{ob,c}	8.9

^aTotal mass in $10^9 \mathfrak{M}_\odot$, reduced to $\Delta=3.1$ Mpc and $i=53^\circ$.

^bFrom photometry.

^cFrom kinematics.

e) Comparison with Other Studies

Previous optical radial velocities of this galaxy have been obtained by Hubble ($V=+286$ km s⁻¹) and by Mayall ($V=+177$ km s⁻¹) (Humason, Mayall, and Sandage 1956) and more recently by Martin (1976) ($V=+200$). Two early 21 cm line velocities reported by Gouguenheim (1969) ($V=+205$ km s⁻¹) and by Robinson ($V=220$ km s⁻¹) (Lewis and Robinson 1973) are superseded by more recent determinations by Whiteoak and Gardner (1977) (WG), Gouguenheim and Bottinelli (1979) (GB), and from H α interferometry by Carranza and Agüero (1977) (CA). Table 10 summarizes the most recent data obtained by the various investigators.

WG find that the p.a. of the line of nodes is 130° , that is, much larger than the p.a. of the major axis (95°), and conclude that the axis of rotation is not normal to the major axis of the galaxy. Their determination may be uncertain in view of the large beamwidth (14'.8) of the Parkes telescope; but if the angle of 130° were correct, it would imply that the p.a. of the line of nodes varies with radius. This could be interpreted by a bending of the galactic plane, as found in radio observations of other spiral galaxies.

GB observe an asymmetry in the distribution of H I: there is more hydrogen in the east ($A=-12.0\pm 1.5$) and in the north ($A=+24\pm 18$). The center of mass is displaced 0.5 ± 0.4 to the east. A is the index of asymmetry introduced by Bottinelli (1971); it measures the percentage excess of mass in one direction. GB estimate that the center of rotation is shifted 0.6 to 0.7 to the east and adopt a systemic velocity of 216 km s⁻¹, while 228 km s⁻¹ is the velocity at the optical center. However, the large fan beam of the Nançay telescope (4' \times 25') makes this conclusion uncertain. We find no compelling evidence in the optical data for either as large a discrepancy between the line of nodes and the major axis, or for a displacement of the rotation center from the optical center.

VI. MODELS FOR THE MASS DISTRIBUTION

In the photometric study of this galaxy (SG VIII), the luminosity distribution was decomposed into an exponential disk of effective radius $a_e^{\text{II}}=2.11$ and an $r^{1/4}$ spheroid of effective radius $a_e^{\text{I}}=6''$ and containing 1.4% of the total blue luminosity. This and the first hump in the rotation curve suggest that a two-component model should be used for the mass distribution in this galaxy.

The rotation curve is well determined only out to r_M , and cannot be supplemented by the radio observations which are at too low resolutions. Hence the slope of the rotation curve in the outer parts of the galaxy remains undetermined; and the total mass of the models, which depends critically on this slope, will be rather uncertain.

a) Thin Disks with Negligible Velocity Dispersions

In a first approximation we neglect the effect of velocity dispersions and consider "cold" models with a fairly round bulge and a flat disk.

An $r^{1/4}$ law with a constant mass-to-light ratio and apparent flattening of 0.4–0.8, even with values of r_e and I_e different from those of the photometry, cannot account for the inner part of the rotation curve.

Adequate bulge models are a spheroid of space density

$$\rho = \rho_c(1 - m^2)^n \quad (6)$$

(Perek 1962), with $n=2$, or a polytrope of index $n=5$, which has the circular velocity given by

$$V^2 = \frac{GM}{a^3} \frac{r^2}{(1+r^2/a^2)^{3/2}} \tag{7}$$

The latter is preferred, since the models with finite velocity dispersions are an extension of it.

Various models have been tried for the disk component: Freeman's thin exponential disk (1970) produces a rotation curve which rises too fast. The photometric model of Monnet and Simien (1977) which uses an exponential disk of finite thickness has the same defect. This means in essence that the mass-to-light ratio varies with distance.

Perek's spheroids (1962) of density $\rho=(1-m^2)^n$ yield curves that rise too slowly. Furthermore, the dimensions of the disks are too small: they end just beyond r_M , unless several spheroids are used to model the disk.

Brandt and Belton's models (1962) of index $n=2-3$ give reasonably good fits. The case $n=2$ is identical to Toomre's model of index $n=0$, and $n=3$ corresponds to the Lohmann-Bottlinger law. The circular velocity of these models is given by

$$V^2 = \frac{GM}{a^3} \frac{r^2}{(1+r^n/a^n)^{3/n}} \tag{8}$$

Except for the case $n=2$, the surface densities must be computed numerically which makes these models inconvenient to use.

The isochrone model of Hénon (1959) used by Eggen, Lynden-Bell, and Sandage (1962) and more recently by Kalnajs (1976) gives a rotation curve which is similar to Brandt and Belton's model of index $n=1.5$ and rises too fast.

The Toomre models (1963) are the most convenient models to obtain a first approximation to the rotation curve. These are thin disks in purely circular rotation with zero velocity dispersion; the circular velocity is given by

$$V_n^2 = \frac{GM}{a} \frac{(n!)^2}{2n!} \frac{r^2}{a^2} \sum_{k=0}^n \frac{(2n-2k)!(2k+1)!}{[k!(n-k)!]^2} \frac{1}{[1+r^2/a^2]^{k+3/2}}, \tag{9}$$

the surface density by

$$\sigma_n = \frac{(2n+1)M}{2\pi a^2} \frac{1}{(1+r^2/a^2)^{n+3/2}} \tag{10}$$

The parameters of the cold models that fit the rotation curve are given in Table 11. The model rotation curve is obtained by adding one bulge and one disk mass model, or the squares of the corresponding circular velocities. The

TABLE 11
PARAMETERS OF MASS DISTRIBUTION MODELS
A. BULGE

Parameter	Perek Spheroid $n=2$	Polytrope $n=5$
a_1 (kpc)	0.8	0.3
c/a	0.5	1.0
M/M_\odot	2.6×10^8	3.5×10^8

B. Disk

Parameter	Lohmann-Bottlinger ^a	Toomre $n=0^b$	Toomre $n=2$	Freeman
a_2 (kpc)	3.00	3.00	5.05	1.764
M/M_\odot	1.14×10^{10}	1.60×10^{10}	8.21×10^9	9.56×10^9

^asame as Brandt-Belton $n=3$.

^bsame as Brandt-Belton $n=2$.

purpose of fitting several models is to give an indication of the accuracy of the mass determination, for given r_M and V_M . The fit is good for the Toomre $n=2$ model and either bulge model, poor for the Freeman disk, and fair for the two others.

Table 11 presents one disturbing fact, namely that the radius containing half the mass of the bulge in projection (the parameter a_1) is very large, more than 3 times larger than the effective radius: that is, the mass distribution needed to account for the rotation curve is much more extended than the luminosity distribution.

Nordsieck (1973) has obtained the same result for a sample of 17 galaxies of various types: "Photometry of central bulges shows that the central mass distribution must be much more centrally concentrated than is indicated by the observed velocity curves, if the mass-to-light ratio is to be physically reasonable."

b) Three-Dimensional Models with Finite Velocity Dispersions

It is possible to resolve in part this apparent conflict by taking into account the velocity dispersions. Such models can become more massive in the center since velocity dispersion (pressure) helps support the galaxy against the gravitational forces.

Gaseous galactic disks are known to be "cold." A typical value for the velocity dispersion normal to the disk is $\sigma_z = 10 \text{ km s}^{-1}$ (Heidmann, Heidmann, and de Vaucouleurs 1971); this is too small to have a noticeable effect on the dynamics.

The situation is very different in the spheroidal component of spiral galaxies. Recently, Whitmore, Kirshner, and Schechter (1979) have measured velocity dispersions in bulges of spiral galaxies and find a dependence on the luminosity of the bulge similar to that found in elliptical galaxies:

$$\log \sigma_r = 0.090 - 0.106 M_T^0, \quad (11)$$

where the constant is for a distance scale assuming $H_0 = 50$. For $H_0 = 100$, the constant is 0.250.

For the bulge of N7793, which has an absolute magnitude $M_T^0 = 14.13 - 27.48 = -13.24$, this relation implies $\sigma_r = 45 \text{ km s}^{-1}$, assuming $H_0 = 100$.

Models with velocity dispersions have been developed by Miyamoto and co-workers (Miyamoto and Nagai 1975; Nagai and Miyamoto 1976; Satoh and Miyamoto 1976) and extended by us to include two-component mass models (see Appendix). The space density in the equatorial plane $z=0$ of a model with a bulge of index $n=0$ and a disk of index $n=2$ is given by:

$$\rho = \frac{\mathfrak{M}_1}{4\pi b X^{5/2}} \left[3b^3 + \frac{5a_1 c_1^2}{X} \left(3b^2 + a_1^2 - 2a_1 b + \frac{7a_1 b c_1^2}{X} \right) \right] + \frac{\mathfrak{M}_2}{4\pi b Y^{3/2}} \left(a_2 + \frac{3bc_2^2}{Y} \right), \quad (12)$$

where $X = r^2 + c_1^2$, $Y = r^2 + c_2^2$, and $c_i = a_i + b$.

The velocity dispersions are given by

$$\sigma_u^2 = \sigma_v^2 = \sigma_w^2 = \frac{b^2}{8\pi G\rho} (T_1^2 + T_2^2), \quad (13)$$

where

$$T_1 = -\frac{G\mathfrak{M}_1}{X^{3/2}} \left[1 + \frac{a_1 c_1}{X} \left(3 + \frac{5a_1 c_1^2}{bX} \right) \right], \quad T_2 = -\frac{G\mathfrak{M}_2 c_2}{bY^{3/2}};$$

the circular velocity V_c by

$$V_c^2 = \frac{G\mathfrak{M}_1 r^2}{X^{3/2}} \left[1 + \frac{a_1}{X} \left(2a_1 + 3b + \frac{5a_1 c_1^2}{X} \right) \right] + \frac{G\mathfrak{M}_2 r^2}{Y^{3/2}}; \quad (14)$$

and the mean velocity of rotation V_0 by

$$V_0^2 = V_c^2 + \frac{b^2 r (T_1 + T_2)}{4\pi G\rho} \left(\frac{\partial T_1}{\partial r} + \frac{\partial T_2}{\partial r} \right), \quad (15)$$

where

$$\frac{\partial T_1}{\partial r} = \frac{G\mathfrak{M}_1 r}{bX^{5/2}} \left[3b + \frac{5a_1 c_1}{X} \left(3b + \frac{7a_1 c_1^2}{X} \right) \right], \text{ and } \frac{\partial T_2}{r} = \frac{3G\mathfrak{M}_2 c_2 r}{bY^{5/2}}.$$

The model that best fits the observations has the following parameters:

Spheroid: $a_1 = 0.04 \text{ kpc}$, $c_1 = 0.14 \text{ kpc}$, $\mathfrak{M}_1/\mathfrak{M}_\odot = 3 \times 10^8$;

Disk: $a_2 = 4.90 \text{ kpc}$, $c_2 = 5.00 \text{ kpc}$, $\mathfrak{M}_2/\mathfrak{M}_\odot = 8 \times 6 \cdot 10^9$.

The mass of the spheroidal component is 3.37% of the total mass.

The ratio $a/(c-a)$ is a measure of the flattening of the components (Nagai and Miyamoto 1976): it is 0.02 for the spheroidal component which is almost round and 2.50 for the disk. Equidensity contours are plotted in Figure 10.

The velocity dispersion at the center is 39.9 km s^{-1} ; it decreases to 8.6 at $r_M = 4.1$. These values are in reasonable agreement with what is to be expected for this galaxy (eq. [11]). The computed rotation curve is in good agreement with the observations (Fig. 9b).

The Toomre criterion (Toomre 1964) for stability against axisymmetric disturbances in a stellar disk, namely that

$$\sigma_u > \frac{3.36\mu(r)}{k},$$

where σ_u is the radial velocity dispersion, $\mu(r)$ is the surface density, and k is the epicyclic frequency, is not satisfied except in the very center of the galaxy. The model is not adequately stabilized by the velocity dispersion alone. The status of this criterion is discussed by Kalnajs (1977).

c) The Mass-to-Light Ratio

In the search for the best mass model, we have been forced to relax the constraints given by the photometry together with the assumption of constant mass-to-light ratio: the distributions of light and matter in a galaxy is too complex to be in a simple constant ratio.

The mass to light ratio $f = \mathfrak{M}/\mathfrak{L}_0$ in the bulge and the disk are given in Table 12 and shown in Figure 11 in two cases: (A) zero, and (B) finite velocity dispersions. In the bulge, the ratio f is more constant in case (B) and in (A). However, because of the drastic variations in this ratio for the bulge taken alone, we suspect that bulge model (B) is still not satisfactory. In the disk, f increases slowly from 0.8 in the center to 2.0 at r_M ; f then increases rapidly. The

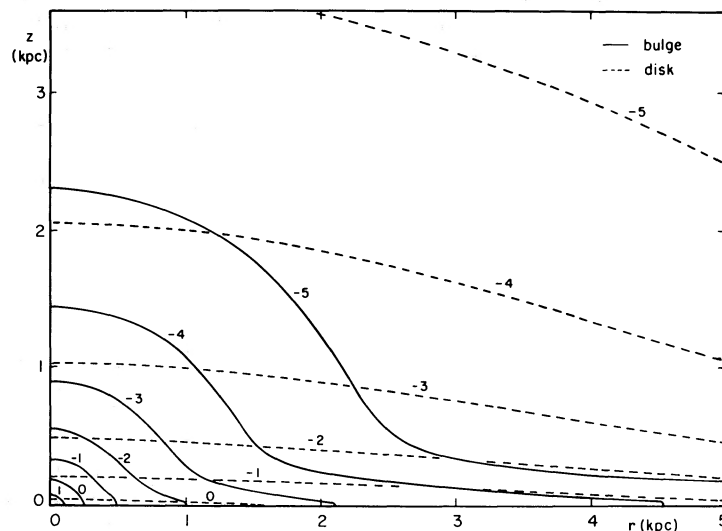


FIG. 10.—Equidensity contours in meridional cross section of two-component model. Log densities in each component in solar masses per cubic parsec. Central densities are $29.6 \mathfrak{M}_\odot \text{ pc}^{-3}$ in bulge, $1.4 \mathfrak{M}_\odot \text{ pc}^{-3}$ in disk.

TABLE 12
MASS-TO-LIGHT RATIOS

Parameter	No Velocity Dispersion	Finite Velocity Dispersion
$\mathfrak{M}_1/\Omega_1^a \dots$	7.69	6.59
$\mathfrak{M}_2/\Omega_2^b \dots$	2.56	2.68
$\mathfrak{M}_T/\Omega_T^c \dots$	2.63	2.74

^a Bulge component.

^b Disk component.

^c Total.

rotation curve beyond r_M is extrapolated, hence very uncertain, but if it is correct, it may be indicative of unseen mass or dark envelope first noted in M31 (de Vaucouleurs 1958) and later in many other systems (for a review, see Faber and Gallagher 1979).

VII. SPECIFIC FEATURES OF THE VELOCITY FIELD

The first cause of perturbations in the axisymmetric velocity field to be expected in a spiral galaxy is a density wave; there is, however, no global pattern in this galaxy, nor spiral filaments of the NGC 2841 type, only short and lumpy spiral arcs. Resonances between the regular pattern arising from a global instability of the disk and individual stellar orbits might explain the absence of global pattern. Other details of interest are noted below.

a) *The Hump in the Rotation Curve*

This hump is evident on both sides of the minor axis, hence it is a real feature of the rotation curve.

The most obvious interpretation is that it is due to the bulge. However, the bulge that is required, even allowing for finite velocity dispersions, is too extended as compared to the photometry and leads to a mass to light ratio that increases outward.

An alternative explanation is to invoke resonance effects, which might perturb the space and velocity distribution of stars at a certain distance from the center. This explanation remains conjectural in the absence of quantitative theoretical predictions.

b) *Difference between Major Axis and Line of Nodes*

There is a difference of 11° between the p.a. of the major axis of the photometric isophotes (SG VIII) and the p.a. of the line of nodes of the galaxy. The two angles were measured with respect to the same reference stars.

If we adopt the p.a. of the major axis to analyze the velocity field we find positive velocity residuals of up to 10 km s^{-1} on the northern side of the major axis and negative residuals of the same amplitude in the south.

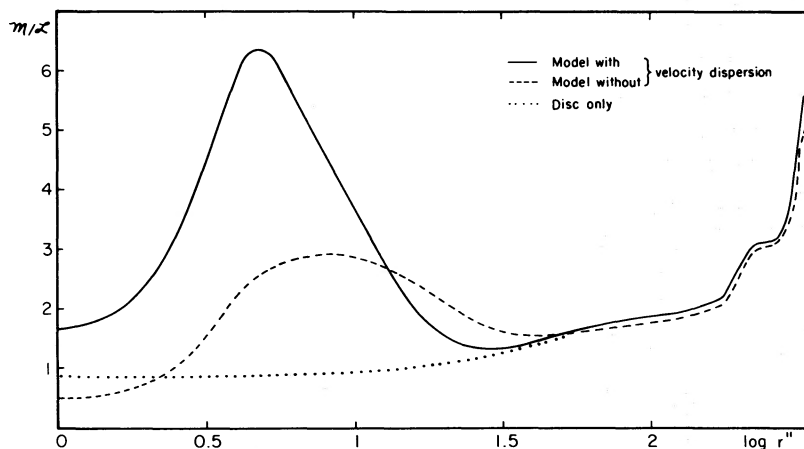


FIG. 11.—Mass-to-light ratio in composite models and in disk

Various interpretations for these residuals are possible:

i) The galaxy is not rotating exactly about its axis of symmetry: it is rotating about its major axis or precessing. The residuals correspond to an angular velocity of $4.9 \text{ km s}^{-1} \text{ kpc}^{-1}$ about the major axis. Such a motion would cause a systematic forced bending of the disk (Lynden-Bell 1965) which is not evident in the photometry.

ii) The galaxy is expanding: if the residual velocities correspond to internal motions in the plane of the galaxy, then the south side (which is the near side) is moving toward us and the north side is moving away from us. The galaxy is expanding with a differential velocity of $5.9 \text{ km s}^{-1} \text{ kpc}^{-1}$. Expansion motions of this order of magnitude or larger have been advocated in other spiral galaxies (van der Kruit and Allen 1978).

Now if the position angle difference is real, two explanations are possible:

i) The gravitational potential is not axisymmetric, and the stellar orbits are elliptical. There is an oval distortion in the disk or a massive nonspherical halo. However, in the absence of evidence for a generating mechanism for such a potential in the photometry, any nonaxisymmetric patterns in the stellar motions will be destroyed by phase mixing after a few rotations (Berry 1973). The rotation period of N7793 is about $2.5 \times 10^8 \text{ yr}$ at r_M .

ii) The plane of the disk is warped: if so, the inclination would change with radial distance, and there is no evidence for this in the photometry or in the kinematics (Table 5).

The two latter explanations are more plausible than the former ones which imply that the galaxy may be disrupted on a short time scale, and the value of $\theta_0 = 108^\circ$ for the position angle of the line of nodes is adopted.

c) Residual Velocities in the Northeast Sector

The observed and calculated velocities contours are compared in Figure 12. The residual velocity field is presented in Figure 13. There are positive residual velocities of up to 25 km s^{-1} in the northeast sector of the galaxy, which is the general direction of the center of the Sculptor group. N45 and N55 are the closest galaxies to N7793; their distances, estimated from the angular separations and relative distance moduli, are 600 kpc and 730 kpc, respectively. Both galaxies are moving away from N7793 with relative radial velocities of 274 and 118 km s^{-1} , respectively.

If these velocities are assumed to be the spatial velocities of the galaxies, they might have had a close encounter with N7793 a few times 10^9 yr ago, which is too long with respect to the rotation period of N7793 to expect lasting effects.

We thank Mrs. A. de Vaucouleurs for her participation in the observations, Dr. M. Créze for helpful advice in the statistical error analysis, and Drs. L. Bottinelli and L. Gougenheim for the communication in advance of publication of their observations of NGC 7793 at 21 cm.

This work was supported in part by NSF grant AST78-08744.

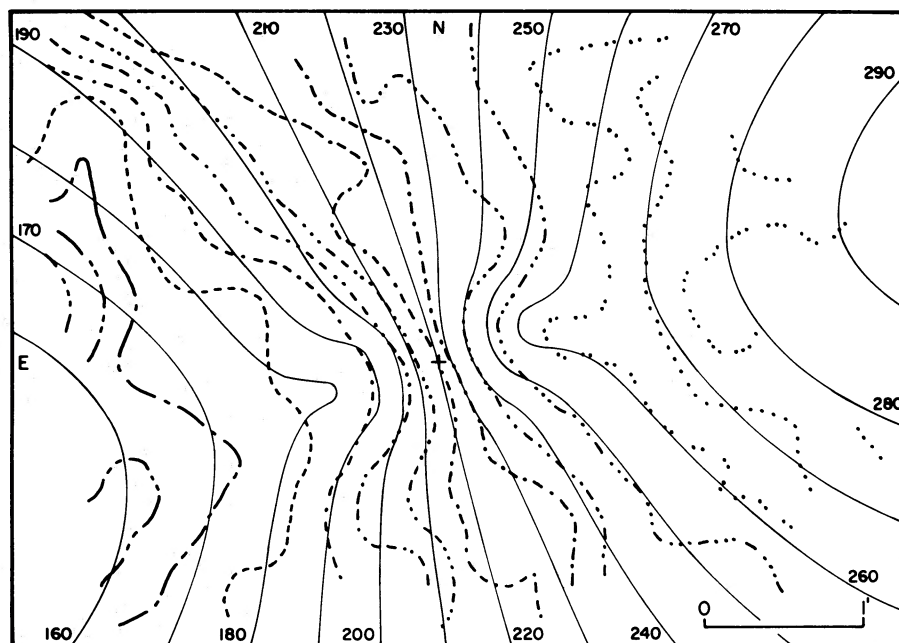


FIG. 12.—Observed and calculated isovelocity curves for adopted model

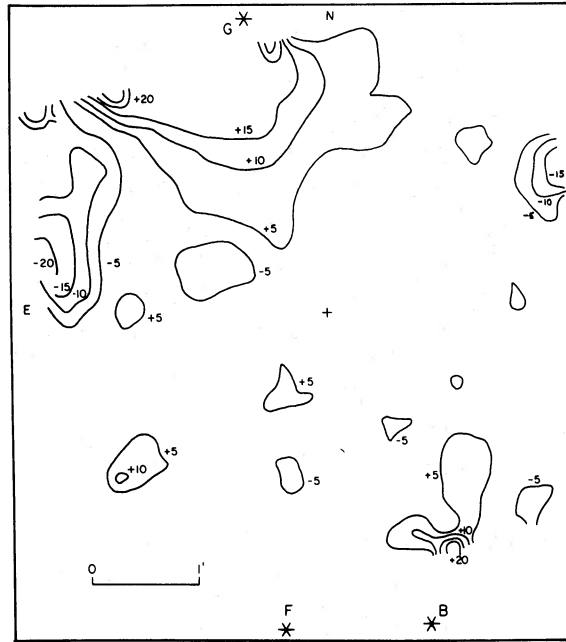


FIG. 13.—Residual velocities from adopted axisymmetric rotation curve

APPENDIX

DYNAMICAL MODEL FOR A TWO-COMPONENT GALAXY WITH A HOT BULGE

The “generalized Toomre models” are three-dimensional mass models for hot or cold disk galaxies that have been developed by Miyamoto and Nagai (1975) and Nagai and Miyamoto (1976) and applied to our Galaxy by Satoh and Miyamoto (1976). We briefly recall their results; the potential of the generalized Toomre model of index n is:

$$\phi = \sum_{k=0}^n \frac{A_{nk} P_k(W)}{k+1}, \quad (\text{A1})$$

where

$$x^2 = z^2 + b^2, \quad R = r^2 + (a+x)^2, \quad W = (a+x)/R^{1/2},$$

$$A_{nk} = \frac{G \mathfrak{M} (2n-k)! a^k (k+1)}{2^{n-k} (2n-1)!! R^{k+1/2} (n-k)!}.$$

$P_k(W)$ is the Legendre polynomial of order k ; r and z are the cylindrical space coordinates, a and b are the free model parameters, \mathfrak{M} is the total mass of the model, G is the gravitational constant.

The corresponding circular velocity v_c , in the absence of velocity dispersion, is given by:

$$V_c^2 = \sum_{k=0}^n A_{nk} [P_k(W) - W P_{k+1}(W)], \quad (\text{A2})$$

and the space density is

$$\rho = \frac{b^2}{4\pi G} \sum_{k=0}^n \frac{A_{nk}}{x^3 R^{1/2}} \left[P_{k+1}(W) + \frac{(k+2) \times P_{k+2}(W)}{R^{1/2}} \right]. \quad (\text{A3})$$

The above equations also hold for a multiple component model. Potentials, densities, and squares of velocities are additive.

We now extend these results to multiple component models with finite velocity dispersions. The mean rotation velocity of a hot disk is obtained by integrating the hydrodynamic equations:

$$\frac{\partial}{\partial r} \rho \langle u^2 \rangle + \frac{1}{r} (\rho \langle u^2 \rangle - \rho \langle v^2 \rangle) = \rho \frac{\partial \phi}{\partial r}, \quad (\text{A4})$$

$$\frac{\partial}{\partial z} \rho \langle w^2 \rangle = \rho \frac{\partial \phi}{\partial z}, \quad (\text{A5})$$

where r , θ , and z are the cylindrical space coordinates and u , v , and w the corresponding velocities. It is simple to verify that the following equation holds true for the generalized Toomre models:

$$\frac{1}{z} \frac{\partial}{\partial z} \left(\frac{1}{z} \frac{\partial \phi}{\partial z} \right) = \frac{4\pi G \rho}{b^2}. \quad (\text{A6})$$

This equality allows us to integrate equation (A5):

$$\rho \langle w^2 \rangle = \frac{b^2}{8\pi G} \left[\frac{1}{z} \frac{\partial \phi}{\partial z} \right]^2 = \frac{b^2 T^2}{8\pi G}, \quad (\text{A7})$$

where

$$T = - \sum_{k=0}^n \frac{A_{nk} P_k(W)}{x R^{1/2}}. \quad (\text{A8})$$

To integrate equation (A4) we assume that there is no third integral of motion at play in the system, or equivalently that the radial and vertical velocity dispersions are equal:

$$\langle u^2 \rangle = \langle w^2 \rangle;$$

hence

$$\langle v^2 \rangle - \langle u^2 \rangle = -r \frac{\partial \phi}{\partial r} + \frac{r}{\rho} \frac{\partial}{\partial r} (\rho \langle u^2 \rangle),$$

$$\langle v^2 \rangle - \langle u^2 \rangle = v_c^2 + \frac{b^2 r T}{4\pi G \rho} \frac{\partial T}{\partial r}, \quad (\text{A9})$$

where

$$\frac{\partial T}{\partial r} = \sum_{k=0}^n \frac{A_{nk}(k+2)}{x r R^{1/2}} [-W P_{k+2}(W) + P_{k+1}(W)]. \quad (\text{A10})$$

It is not possible to find the mean rotation velocity v_0 without any additional assumption about the velocity distribution in the galaxy. We assume that the dispersion of residual velocities is isotropic:

$$\langle u^2 \rangle = \langle v^2 \rangle - v_0^2 = \langle w^2 \rangle.$$

This assumption is probably valid in the bulge, but rather poor in the outer disk. However, as noted by Nagai and Miyamoto (1976), the effect of finite velocity dispersions on the rotation curve of a thin disk ($b/a \ll 1$) is negligible. The mean rotation velocity is then

$$v_0^2 = v_c^2 + \frac{b^2 r T}{4\pi G \rho} \frac{\partial T}{\partial r}. \quad (\text{A11})$$

Equations (A6)–(A11) remain valid for a multiple component model provided the parameter b is the same for all components. Potentials, densities, and square velocities are additive.

REFERENCES

- Berry, C. L. 1973, *Ap. J.*, **179**, 395.
 Boeshaar, G. O., and Hodge, P. W. 1977, *Ap. J.*, **213**, 361.
 Bosma, A. 1978, Ph.D. dissertation, University of Groningen.
 Bottinelli, L. 1971, *Astr. Ap.*, **10**, 437.
 Brandt, J. C., and Belton, M. J. S. 1962, *Ap. J.*, **136**, 352.
 Carranza, G. J., and Aguero, E. 1977, *Ap. Space Sci.*, **47**, 397.
 de Vaucouleurs, G. 1958, *Ap. J.*, **128**, 465.
 ———. 1959, *Ap. J.*, **130**, 718.
 ———. 1977, in *The Evolution of Galaxies and Stellar Populations*, ed. B. M. Tinsley and R. B. Larson (New Haven: Yale University Obs.), p. 43.
 de Vaucouleurs, G., and Davoust, E. 1980, *Ap. J.*, in press (SG VIII).
 de Vaucouleurs, G., and Pence, W. 1980, *Ap. J.*, **242**, 18, (Paper I).
 Eggen, O. J., Lynden-Bell, D., and Sandage, A. 1962, *Ap. J.*, **136**, 748.
 Faber, S. M., and Gallagher, J. S. 1979, *Ann. Rev. Astr. Ap.*, **17**, 135.
 Freeman, K. C. 1970, *Ap. J.*, **160**, 811.
 Gouguenheim, L. 1969, *Astr. Ap.*, **3**, 281.
 Gouguenheim, L., and Bottinelli, L. 1979, private communication (GB).
 Heidmann, J., Heidmann, N., and de Vaucouleurs, G. 1971, *Mem. R.A.S.*, **75**, 85.
 Hénon, M. 1959, *Ann. d'Ap.*, **22**, 126.
 Hodge, P. W. 1969a, *Ap. J. Suppl.*, **18**, 73.
 ———. 1969b, *Ap. J.*, **155**, 417.
 Humason, M., Mayall, N., and Sandage, A. 1956, *A.J.*, **61**, 97.
 Kalnajs, A. J. 1976, *Ap. J.*, **205**, 751.
 ———. 1977, in *IAU Symposium 77, Structures and Properties of Nearby Galaxies*, ed. E. M. Berkhuijsen and R. Wielebinski (Boston: Reidel), p. 113.
 Kennicutt, R. C., and Hodge, P. W. 1976, *Ap. J.*, **207**, 36.
 Lewis, B. M., and Robinson, B. J. 1973, *Astr. Ap.*, **23**, 295.
 Lynden-Bell, D. 1965, *M.N.R.A.S.*, **129**, 299.
 Martin, W. L. 1976, *M.N.R.A.S.*, **175**, 633.
 Miyamoto, M., and Nagai, H. 1975, *Pub. Astr. Soc. Japan*, **27**, 533.
 Monnet, G. 1971, *Astr. Ap.*, **12**, 379.
 Monnet, G., and Simien, F. 1977, *Astr. Ap.*, **56**, 173.
 Nagai, H., and Miyamoto, M. 1976, *Pub. Astr. Soc. Japan*, **28**, 1.
 Nordsieck, K. H. 1973, *Ap. J.*, **184**, 719.
 Perek, L. 1962, in *Advances in Astronomy and Astrophysics* (New York: Academic Press), p. 165.
 Satoh, C., and Miyamoto, M. 1976, *Pub. Astr. Soc. Japan*, **28**, 599.
 Shapley, H. 1943, *Galaxies* (Philadelphia: Blakiston), p. 29.
 Toomre, A. 1963, *Ap. J.*, **138**, 385.
 ———. 1964, *Ap. J.*, **139**, 1217.
 van der Kruit, P. C., and Allen, R. J. 1978, *Ann. Rev. Astr. Ap.*, **16**, 103.
 Warner, P. J., Wright, M. C. H., and Baldwin, J. E. 1973, *M.N.R.A.S.*, **163**, 163.
 Whiteoak, J. B., and Gardner, F. F. 1977, *Australian J. Phys.*, **30**, 187 (WG).
 Whitmore, B. C., Kirshner, R. P., and Schechter, P. 1979, *Ap. J.*, **234**, 68.

G. DE VAUCOULEURS: Department of Astronomy, The University of Texas, Austin, TX 78712

E. DAVOUST: Observatoire de Besançon, 25000 Besançon, France.

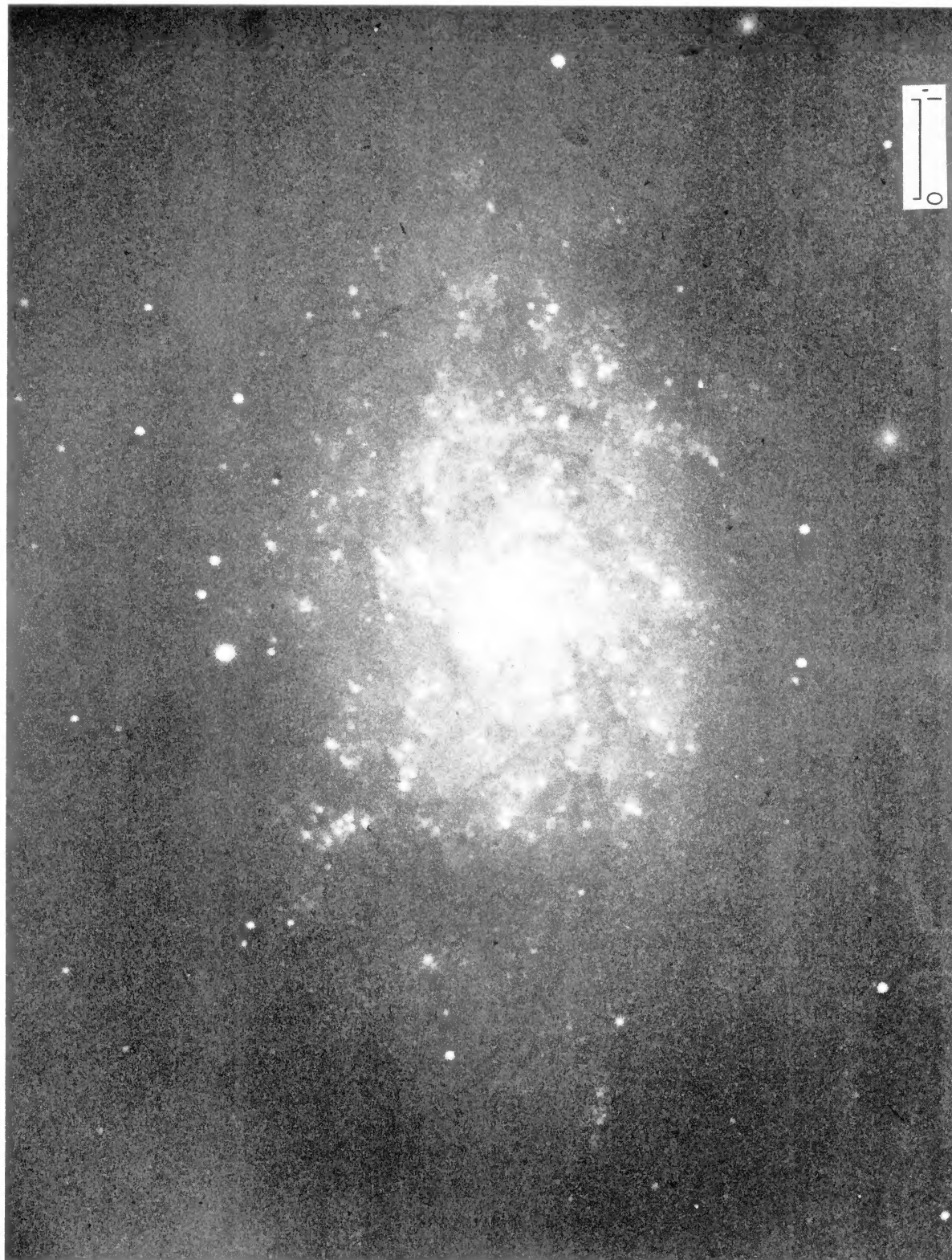
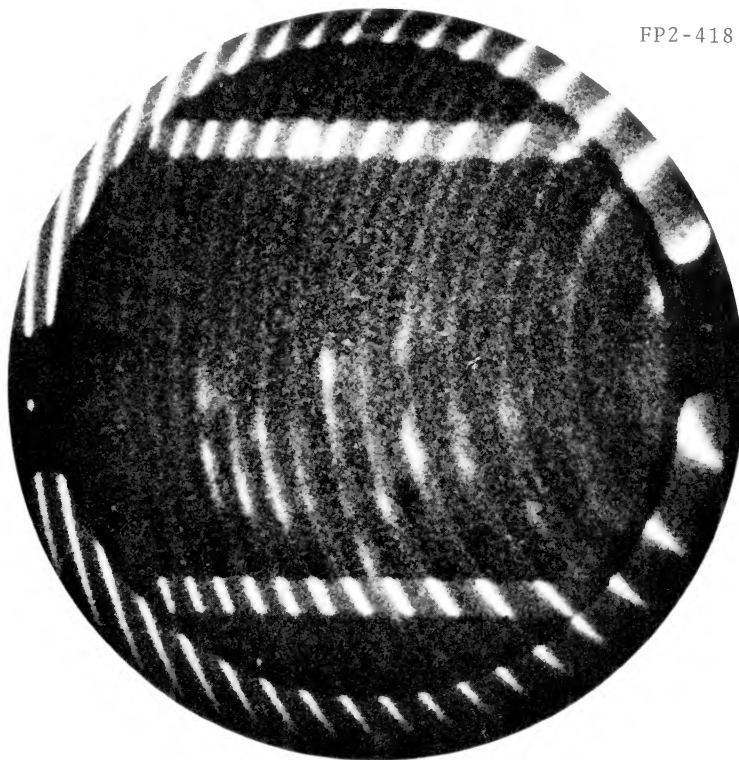


FIG. 1.—Photograph of NGC 7793 in blue light with 406/135 mm $f/4.8$ reducing camera at Cassegrain focus of McDonald 205 cm Struve reflector (1978 Oct. 5, pre-flashed IIa-O, 60 min).

DAVOUST AND DE VAUCOULEURS (*see* page 30)

PLATE 2

FP2-418



FP2-419

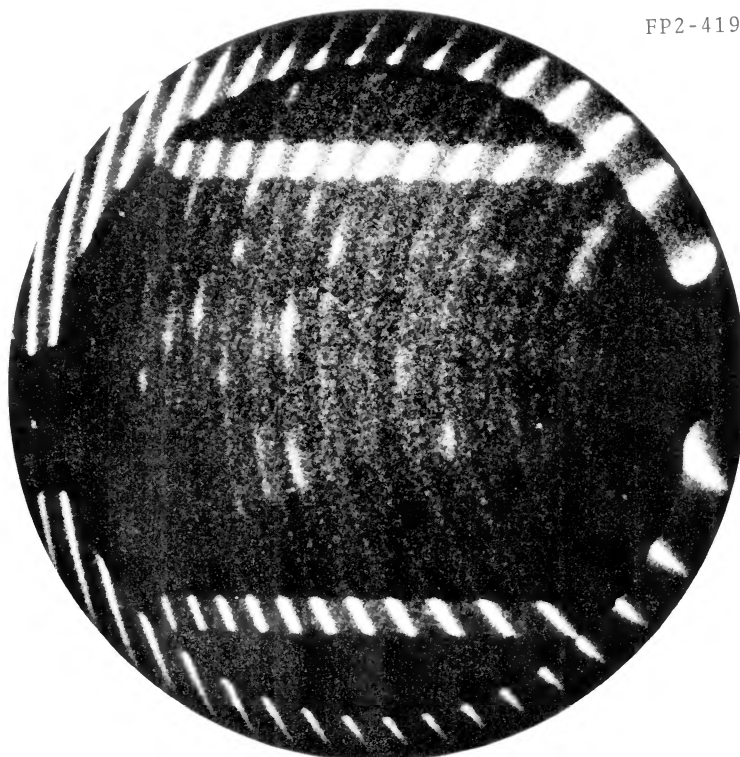


FIG. 2.—Examples of interferograms of NGC 7793. Fields, 3.5 in diameter, are centered 2:1 NE (418) and 2:1 SE (419) of nucleus (see Table 1). Exposure times: 45 min on preflashed 103a-G film with gas-cooled two-stage Varo S20VR image tube at 23 kV on Galaxymer at Cassegrain focus of Struve reflector. Note additional calibration windows and contamination by zero-velocity $H\alpha$ and, in upper part of field, by airglow $\lambda 6577$ OH line.

DAVOUST AND DE VAUCOULEURS (*see* page 31)

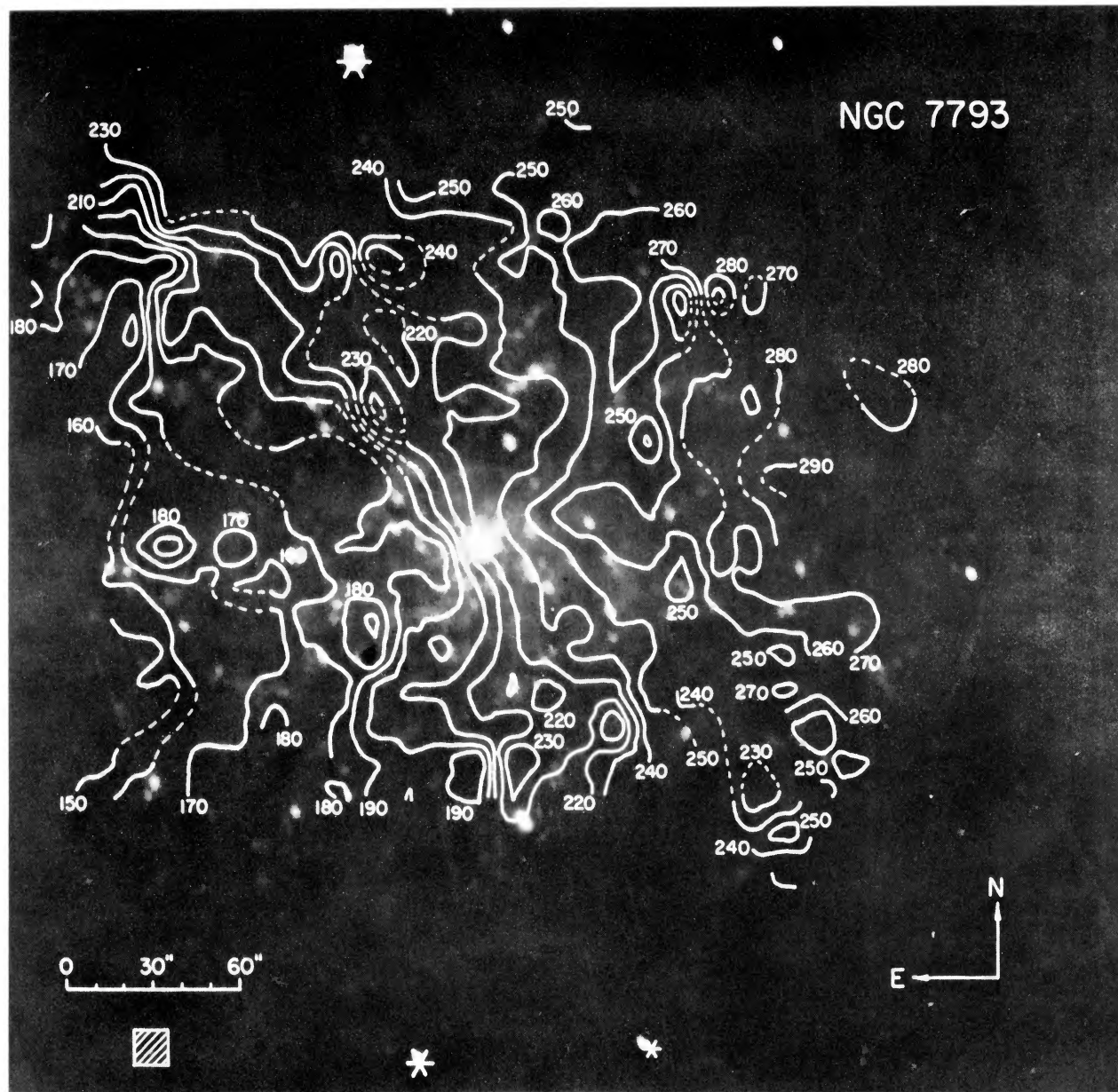


FIG. 6.—Velocity field in NGC 7793 before interpolation and smoothing superimposed on B-band photograph of galaxy. Hatched square shows pixel size.

DAVOUST AND DE VAUCOULEURS (*see* page 38)

PLATE 4

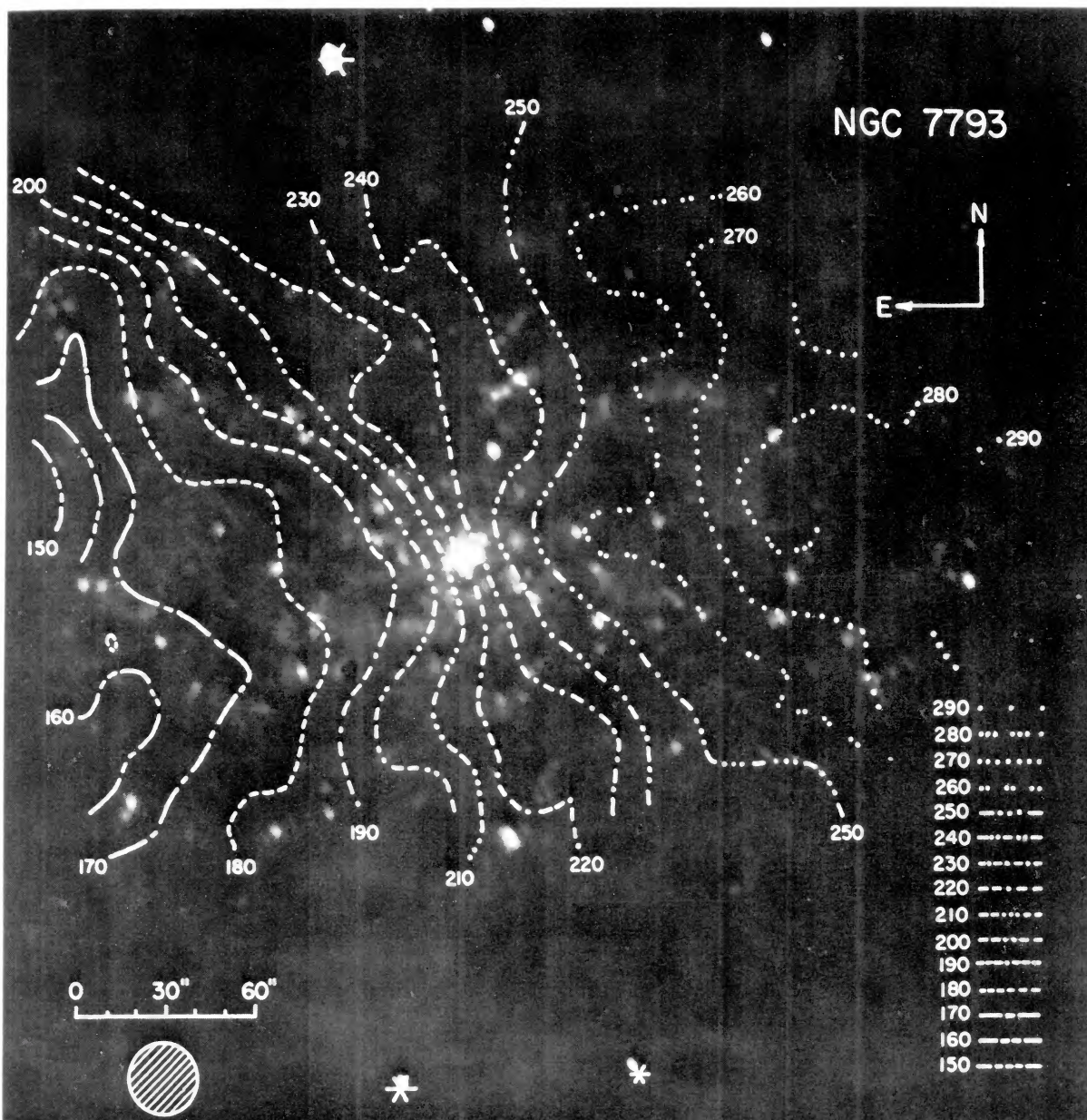


FIG. 7.—Velocity field in NGC 7793 after interpolation and smoothing. Hatched circle shows effective (half total power) diameter of smoothing beam.

DAVOUST AND DE VAUCOULEURS (see page 38)